Publicly Accessible Penn Dissertations

2007

Nuclear magnetic resonance studies of local magnetic, electronic, and dynamic properties in filled single wall carbon nanotubes

Younghyun Kim

Follow this and additional works at: https://repository.upenn.edu/edissertations

Part of the Materials Science and Engineering Commons

Recommended Citation

Nuclear magnetic resonance studies of local magnetic, electronic, and dynamic properties in filled single wall carbon nanotubes

Abstract

In this dissertation, the local magnetic and electronic properties of SWNTs are investigated. Also, one dimensional (1-D) dynamics of C60 fullerenes encapsulated in SWNTs is investigated using Nuclear Magnetic Resonance (NMR) spectroscopy. In order to remove ferromagnetic catalyst particles present in SWNT samples, which interfere with NMR measurements, we have developed a novel magnetic purification method by which 99% of the ferromagnetic particles are removed. With this new method, we could obtain a well-resolved NMR signal with FWHM of ~20 ppm from natural carbon based SWNTs. Using 25% 13C enriched C60 encapsulated in the magnetically purified SWNTs as an NMR probe, the local magnetic properties of the 1-D inner space of SWNTs are studied. Surprisingly, SWNTs are found to screen the applied magnetic field by tens of ppm. More interestingly, the diamagnetic shielding is found to be tunable by controlling defects or doping. While defects create paramagnetic currents to destroy the diamagnetic shielding, doping enhances the shielding by increase aromaticity in SWNTs to have stronger diamagnetic ring currents. Encapsulated fullerenes in SWNTs show unique dynamics which is related to 1-D geometry. They are found to undergo dynamics transition from free rotation to hindered rotation at ~100 K, which is lower than that in 3-D bulk fullerenes by as much as ~160 K. This huge reduction results from the decrease of Van der Waals interaction and the Coulomb interaction between an electron-rich bond and an electron-poor center of a pentagon or a hexagon. DWNTs were made by high temperature annealing of enriched peapods. The isotropic chemical shift of inner nanotubes was found to have shifted diamagnetically by 26.62 ppm due to the magnetic shielding by outer nanotubes. 75% of the inner nanotubes were proven to be metallic due to a strong interaction between inner and outer nanotubes.

Degree Type
Dissertation

Degree Name
Doctor of Philosophy (PhD)

Graduate Group
Materials Science & Engineering

First Advisor
David E. Luzzi

Keywords
Applied sciences, Dynamics of fullerenes inside nanotubes, Fullerenes, Local magnetic properties of SWNTs, NMR, Nanotubes, Peapods

Subject Categories
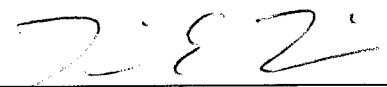Materials Science and Engineering

NUCLEAR MAGNETIC RESONANCE STUDIES OF

LOCAL MAGNETIC, ELECTRONIC, AND DYNAMIC PROPERTIES

IN FILLED SINGLE WALL CARBON NANOTUBES

Younghyun Kim

A DISSERTATION

in

Materials Science and Engineering

Presented to the Faculties of the University of Pennsylvania in Partial
Fulfillment of the Requirements for the Degree of Doctor of Philosophy

2007

_____

Supervisor of Dissertation

_____

Graduate Group Chairperson

UMI Number: 3292040

INFORMATION TO USERS

The quality of this reproduction is dependent upon the quality of the copy submitted. Broken or indistinct print, colored or poor quality illustrations and photographs, print bleed-through, substandard margins, and improper alignment can adversely affect reproduction.

In the unlikely event that the author did not send a complete manuscript and there are missing pages, these will be noted. Also, if unauthorized copyright material had to be removed, a note will indicate the deletion.

UMI®

To my family and Lim

ACKNOWLEDGEMENTS

graduation. Sincerely, I thank my advisor Prof. Jong-Wan Park for his heartful mentoring, without which, my successful graduation would not have been possible today.

Above all, my deepest/biggest thanks with whole of my heart are given to my father Chul Gyun Kim and mother Ok Ja Lee. To my sister and brothers, "thank you very much too :)". Lastly, I thank my fiancé, Jeong Lim Kang, for all the happiness she brings into my life. I love you!

ABSTRACT

NUCLEAR MAGNETIC RESONANCE STUDIES OF

LOCAL MAGNETIC, ELECTRONIC, AND DYNAMIC PROPERTIES

IN FILLED SINGLE WALL CARBON NANOTUBES

Younghyun Kim

Supervisor: David E. Luzzi

In this dissertation, the local magnetic and electronic properties of SWNTs are investigated. Also, one dimensional (1-D) dynamics of C_{60} fullerenes encapsulated in SWNTs is investigated using Nuclear Magnetic Resonance (NMR) spectroscopy. In order to remove ferromagnetic catalyst particles present in SWNT samples, which interfere with NMR measurements, we have developed a novel magnetic purification method by which 99% of the ferromagnetic particles are removed. With this new method, we could obtain a well-resolved NMR signal with FWHM of ~20 ppm from natural carbon based SWNTs. Using 25% ^{13}C enriched C_{60} encapsulated in the magnetically purified SWNTs as an NMR probe, the local magnetic properties of the 1-D inner space of SWNTs are studied. Surprisingly, SWNTs are found to screen the applied magnetic field by tens of ppm. More interestingly, the diamagnetic shielding is found to be tunable by controlling defects or doping. While defects create paramagnetic currents to destroy the diamagnetic shielding, doping enhances the shielding by increase aromaticity in

SWNTs to have stronger diamagnetic ring currents. Encapsulated fullerenes in SWNTs show unique dynamics which is related to 1-D geometry. They are found to undergo dynamics transition from free rotation to hindered rotation at ~ 100 K, which is lower than that in 3-D bulk fullerenes by as much as ~ 160 K. This huge reduction results from the decrease of Van der Waals interaction and the Coulomb interaction between an electron-rich bond and an electron-poor center of a pentagon or a hexagon. DWNTs were made by high temperature annealing of enriched peapods. The isotropic chemical shift of inner nanotubes was found to have shifted diamagnetically by 26.62 ppm due to the magnetic shielding by outer nanotubes. 75% of the inner nanotubes were proven to be metallic due to a strong interaction between inner and outer nanotubes.

TABLE OF CONTENTS

LIST OF TABLES

LIST OF FIGURES

CHAPTER 1

INTRODUCTION

1.1 NUCLEAR MAGNETIC RESONANCE (NMR) TO PROBE THE INNER SPACE OF SWNTs

In 1991, Iijima discovered a new carbon molecular structure, called multi-wall carbon nanotubes (MWNTs), which are composed of many layers of rolled graphene sheets [1]. Despite the expectation of interesting one dimensional (1-D) properties, the usual diameter of MWNTs, spanning in the range of 10-50 nm, turned out to be too large for these properties. Not long after the MWNT discovery, single wall carbon nanotubes (SWNTs), whose diameter is as small as 0.4 nm, were discovered, which makes them behave as a true 1-D material [2,3].

Various theoretical and experimental studies have confirmed the unique 1-D related physics in SWNTs. Electrical measurements and optical spectroscopy have confirmed the presence of van Hove singularities in SWNTs, which indicate the degenerate density of states (DOS) in the band edges of each 1-D energy band [4-9]. It is surprising that despite the similar chemical composition, their electronic properties could be metallic or semiconducting depending on which geometry they are wrapped from a graphene layer [10]. Tomonaga-Luttinger-liquid (TLL) behavior was verified in metallic SWNTs where the 3-D Fermi-liquid theory breaks down due to the strong correlation between the electrons [11-13]. SWNTs have been proven to become quantum dots

(CNTQDs) in applied magnetic fields where electron wave vectors in a SWNT 1-D box are quantized due to quantum confinement along the radial direction [5]. SWNTs have been investigated in spintronics field as an electronic transport medium since the 1-D electronic transport is ballistic and spin-orbit relaxation is negligible, resulting in a long mean free path [14-18].

In addition to their unique 1D properties, there is another special characteristic of SWNTs which has not been explored yet. That is the inner 1-D space which can be used as physically and chemically intact nano-space, which affords unique experiments. As SWNTs themselves have been proven to show various 1-D characteristics, inner space can be used as a template to study 1-D properties of materials of interest, which could be distinctly different from their 3-D properties [19]. A perfect example of the 1-D space utilization so far is the fullerene C_{60} filled SWNTs, called as 'peapods', which were discovered by Luzzi and coworkers [20,21]. While fullerenes in 3-D bulk solid have 12 nearest neighbors at room temperature, they can have only 2 nearest neighbors in case of peapods, which in turn could affect the physical properties in 3D, such as the phase transition temperature or dynamics [22-25].

Along with the fundamental interest, the inner space in SWNTs can be used for various applications. For example, SWNTs can be used for gas storage for the next generation synthetic fuel [26,27]. Biologically, they can be used as nano-needles to deliver drug to a specific location without destroying cells [28]. A transition metal 1-D wire encapsulated in SWNTs can also be used as an advanced memory device or as a

conducting wire needed for high density magnetic storage, while encapsulating SWNTs prevent the degradation of the encapsulated materials from the atmosphere [29].

For both fundamental interest and application purpose, it is necessary to study local magnetic fields of SWNTs. Nuclear Magnetic Resonance (NMR) spectroscopy is an excellent tool for the purpose. Electronic properties and the molecular dynamics of encapsulated materials can also be studied using NMR. In this thesis, the local magnetic properties of SWNTs, the 1-D dynamics of encapsulated C_{60} inside SWNTs, and the electronic properties of inner nanotubes in DWNTs have been investigated systematically using NMR technique.

1.2 HISTORY AND CHALLENGES OF NMR OF SWNTs

In order to study the local magnetic properties of SWNTs and 1-D fullerene dynamics inside SWNTs, the SWNT samples for NMR need to meet certain requirements. There should be no transition metal catalyst particles present, to get a uniform magnetic field inside the sample. A large enough diameter for SWNTs is a must, in order to introduce C_{60} fullerenes, and mass scale production of clean SWNT samples is required, as NMR measurements need large amount of sample. Ferromagnetic catalyst particles, which are used for SWNT production, destroy the homogeneous magnetic field inside a sample, thus broadening the NMR signal to be analyzed [30]. To circumvent this problem, Tang *et al.* used non-ferromagnetic metals, such as Rh/Pd, as catalyst particles for SWNTs [31]. They found a single isotropic chemical shift at 124 ppm despite the

3

prediction that metallic and semiconducting SWNTs would result in different chemical shifts [32,33]. From a spin-lattice relaxation time measurement, they found two different relaxation sources, confirming that one third of SWNTs is metallic and the other two thirds are semiconducting in their sample. Despite the successful NMR measurement, Rh/Pd catalyst based SWNTs have a huge drawback because the average diameter of 0.8 nm is too small to introduce C_{60}.

In liquid-state NMR studies, isotropic chemical shifts of metallic and semiconducting SWNTs could be resolved to be 110 and 120 ppm, respectively [34]. Metallic tubes are confirmed to have ~ 10 ppm of Knight shift compared to semiconducting nanotubes due to conduction electrons at the Fermi level [33]. In order to increase the NMR signal intensity, they used ^{13}C enriched SWNTs, whose transition metal catalyst particles were removed by magnetic processing, using standard techniques common to biochemical fields. However, these purification methods are still insufficient to achieve the levels of purity necessary for electric and thermal applications and for the study of standard non-enriched nanotube materials. The high cost and low yield of SWNT materials provided by these methods make them ill-suited for mass production.

From ^{1}H NMR studies, Kleinhammes *et al.* claimed that the inner space of SWNTs becomes available for methane or ethane absorption after opening SWNTs [35]. Matsuda *et al.* studied dynamics of water encapsulated in SWNTs, and observed that the movement of the water starts to be restricted below 220 K, followed by a total frozen state below 120 K [36]. Both groups, however, used only static NMR and relaxation measurements for their studies without magic angle spinning (MAS) NMR, which can

give detailed local magnetic properties of SWNTs. It should be noted that only a small amount of ferromagnetic catalyst particles could broaden the MAS-NMR signal, destroying the fine structure of an isotropic chemical shift.

Apart from NMR measurements, ferromagnetic catalyst particles used for SWNT production have been huge obstacle for various other characterization methods. For example, the electron spin resonance (ESR) signal is absent in catalyst-containing samples, because the excited electron spins are relaxed instantly in the vicinity of ferromagnetic catalyst particles before they are detected [37,38]. The measurement of the specific heat is obscured at a low temperature because of nuclear hyperfine interactions in metallic impurities [39]. Small amounts of magnetic impurities can also influence nanotube electrical properties through Kondo-like interactions with conduction electrons [40,41].

Various purification methods have been employed to remove magnetic catalyst impurities [42-45]. Rinzler *et al.* used nitric acid refluxing to remove amorphous carbon or defective graphitic layers coating metal particles and then dissolve the bare metal [42]. The method, however, could not remove especially large catalyst particles as they are coated with thick graphitic layers. Harutyunyan *et al.* used microwave heating by which graphitic layers coating large metal particles are first removed, followed by a mild acid treatment to dissolve the residual metal [44]. However, the method has drawbacks of low yield and damage to SWNTs themselves. Several groups have employed magnetic filtration to attract ferromagnetic catalyst particles, but the efficiency is so low that

ferromagnetism still dominated the magnetic moment of the sample for magnetic fields of the order a few Tesla [46-49].

Despite such various purification methods, SWNTs which satisfy the requirements for NMR studies, mentioned earlier have not been available yet. A novel purification method, therefore, needs to be developed, which is efficient enough to remove most of the ferromagnetic catalyst particles to get a sharp NMR signal. The purification method needs to be gentle enough not to change or destroy SWNT structure, simple enough to be applied to all kinds of SWNT materials, including 1.4 nm diameter SWNTs used for making peapods. Finally, the purification approach should be scalable to produce massive quantities of purified SWNTs for NMR measurement ($\geq$30 mg).

1.3 THESIS OVERVIEW

In the first chapter, the goal of this thesis is described, which relates to the NMR studies of the local magnetic properties of SWNTs, 1-D dynamics of encapsulated C_{60}, and the electronic properties of inner nanotubes in DWNTs. The scientific problems involved are described with the motivation, history, and challenges in the field. In chapter 2, the basic properties of SWNTs, such as electronic, optical, vibrational, and magnetic properties will be mentioned, followed by the basic theory, chemical shift, and relaxation mechanisms in NMR technique. Chapter 3 describes the novel purification approach using magnetic filtration by which over 99% of ferromagnetic catalyst particles were removed to produce a diamagnetic SWNT sample. In chapter 4, using ^{13}C enriched-C_{60}

6

filled purified SWNT peapods, local magnetic fields of SWNTs, 1-D dynamics of fullerenes, and the electronic properties of inner nanotubes in DWNTs will be examined. In chapter 5, the effect of defects and doping on the local magnetic property of SWNTs will be elaborated. Finally, in chapter 6, a summary of the current work and the future prospects will follow.

1. S. Iijima, Nature **354**, 56 (1991).

2. S. Iijima, and T. Ichihashi, Nature **363**, 603 (1993).

3. L. Qin, X. Zhao, K. Hirahara, Y. Miyamoto, Y. Ando, and S. Iijima, Nature **408**, 50 (2000).

4. S. J. Tans, M. H. Devoret, R. J. A. Groeneveld, and C. Dekker, Nature **394**, 761 (1998).

5. E. D. Minot, Y. Yaish, V. Sazonova, and P. L. McEuen, Nature **428**, 536 (2004).

6. P. Delaney, H. J. Choi, J. Ihm, S. G. Louie, and M. L. Cohen, Nature **391**, 466 (1998).

7. S. J. Tans, A. R. M. Verschueren, and C. Dekker, Nature **393**, 49 (1998).

8. S. M. Bachilo, M. S. Strano, C. Kittrell, R. H. Hauge, R. E. Smalley, and R. Bruce Weisman, science **298**, 2361 (2002).

9. M. E. Itkis, S. Niyogi, M. E. Meng, M. A. Hamon, H. Hu, and R. C. Haddon, Nano Lett. **2**, 155(2002).

10. R. Saito, M. Fujita, G. Dresselhaus, and M. S. Dresselhaus, Appl. Phys. Lett. **60**, 2204(1992).

11. H. Ishii, H. Kataura, H. Shiozawa, H. Yoshioka, H. Otsubo, Y. Takayama, T. Miyahara, S. Suzuki, Y. Achiba, M. Nakatake, T. Narimura, M. Higashiguchi, K. Shimada, H. Namatame, and M. Taniguchi, Nature **426**, 540 (2003).

12. C. Kane, L. Balents, and M. P. A. Fisher, Phys. Rev. Lett. **79**, 5086 (1997).

13. H. Rauf, T. Pichler, M. Knupfer, J. Fink, and H. Kataura, Phys. Rev. Lett. **93**, 096805 (2004).

14. A. Javey, J. Guo, Q. Wang, M. Lundstrom, and H. Dai, Nature **424**, 654 (2003).

15. K. Tsukagoshi, B. W. Alphenaar, and H. Ago, Nature **401**, 572 (1999).

16. J.-R. Kim, H. M. So, J.-J. Kim, and J. Kim, Phys. Rev. B **66**, 233401 (2002).

17. A. Jensen, J. R. Hauptmann, J. Nygård, and P. E. Lindelof, Phys. Rev. B **72**, 035419 (2005).

18. S. Rocheand, and R. Saito, Phys. Rev. Lett. **87**, 246803 (2001).

19. M. M. Calbi, M. W. Cole, S. M. Gatica, M. J. Bojan, and G. Stan, Rev. Mod. Phys. **73**, 857 (2001).

20. D. J. Hornbaker, S.-J. Khang, S. Misra, B. W. Smith, A. T. Johnson, E. J. Mele, D. E. Luzzi, and A. Yazdani, Science **295**, 828 (2002).

21. B. W. Smith, M. Monthioux, and D. E. Luzzi, Nature **396**, 323 (1998).

22. P. A. Heiney, J. E. Fischer, A. R. McGhie, W. J. Romanow, A. M. Denenstein, J. P. McCauley, Jr., and A. B. Smith, Phys. Rev. Lett. **66**, 2911(1991).

23. R. Tycko, G. Dabbagh, R. M. Fleming, R. C. Haddon, A. V. Makhija, and S. M. Zahurak, Phys. Rev. Lett. **67**, 1886 (1991).

24. R. Blinc, J. Seliger, J. Dolinsek, and D. Arcon, Phys. Rev. B **49**, 4993(1994).

25. M. Hodak, and L. A. Girifalco, Phys. Rev. B **68**, 085405 (2003).

26. A. C. Dillon, K. M. Jones, T. A. Bekkedahl, C. H. Kiang, D. S. Bethune, and M. J. Heben, Nature **386**, 377 (1997).

27. L. Schlapbach, and A. Züttel, Nature **414**, 353 (2001).

28. A. Bianco, K. Kostarelos, and M. Prato, Curr. Opin. Chem. Biol. **9**, 674(2005).

29. Y. F. Li, R. Hatakeyama, T. Kaneko, T. Izumida, T. Okada, and T. Kato, Appl. Phys. Lett. **89**, 083117 (2006).

30. M. H. Levitt, *Spin dynamics-basics of nuclear magnetic resonance*, John Wiley & Sons, LTD, New York (2001).

31. X. P.Tang, A. Kleinhammes, H. Shimoda, L. Fleming, K. Y. Bennoune, S. Sinha, C. Bower, O. Zhou, and Y. Wu, Science **288**, 492 (2000).

32. N. A. Besley, J. J. Titman, and M. D. Wright, J. Am. Chem. Soc., **127**, 17948 (2005).

33. S. Latil, L. Henrard, C. Goze Bac, P. Bernier, and A. Rubio, Phys. Rev. Lett. **86**, 3160 (2001).

34. A. Kitaygorodskiy, W. Wang, S-Y. Xie, Y. Lin, K. A. Shiral Fernando, X. Wang, L. Qu, B. Chen, and Y-P. Sun, J. Am. Chem. Soc. **127**, 7517 (2005).

35. A. Kleinhammes, S.-H. Mao, X.-J. Yang, X.-P. Tang, H. Shimoda, J. P. Lu, O. Zhou, and Y. Wu, Phys. Rev. B **68**, 075418 (2003).

36. K. Matsuda, T. Hibi, H. Kadowaki, H. Kataura, and Y. Maniwa, Phys. Rev. B **74**, 073415 (2006).

37. A. S. Claye, N. M. Nemes, A. Janossy, and J. E. Fischer, Phys. Rev. B, **62**, R4845 (2000).

38. B. Nafradi, N. Names, T. Feher, L. Forro, Y. Kim, J. E. Fisher, D. E. Luzzi, F. Simon, and H. Kuzmany, Phy. Stat. Sol. (b) **243** (13), 3106 (2007).

39. J. C. Lasjaunias, K. Biljakovic, Z. Benes, J. E. Fischer, and P. Monceau, Phy. Rev. B **65**, 113409 (2002).

40. L. Grigorian, G. U. Sumanasekera, A. L. Loper, S. L. Fang, J. L. Allen, and P. C. Eklund, Phys. Rev. B **60**, R11309 (1999).

41. R. S. Gracia, T. M. Nieuwenhuizen, and I. V. Lerner, Europhys. Lett. **66**, 419 (2004).

42. A. G. Rinzler, J. Liu, H. Dai, P. Nikolaev, C. B. Huffman, F. J. Rodriguez-Macias, P. J. Boul, A. H. Lu, D. Heymann, D. T. Colbert, R. S. Lee, J. E. Fischer, A. M. Rao, P. C. Eklund, and R. E. Smalley, App. Phy. A **67**, 29 (1998).

43. K. L. Strong, D. P. Anderson, K. Lafdi, and J. N. Kuhn, Carbon **41**, 1477 (2003).

44. A. R. Harutyunyan, B. K. Pradhan, J. Chang, G. Chen, P. C. Eklund, J. Phys. Chem. B **106**, 8671 (2002).

45. W. Zhou, Y. H. Ooi, R. Russo, P. Papanek, D. E. Luzzi, J. E. Fischer, M. J. Bronikowski, P. A. Willis, and R. E. Smalley, Chem. Phys. Lett **350**, 6 (2001).

46. L. Thien-Nga, K. Hernadi, E. Ljubovic, S. Garaj, and L. Forro, Nano Lett. **2**, 1349 (2002).

47. J. G. Wiltshire, L. J. Li, A. N. Kholbystov, C. J. Padbury, G. A. D. Briggs, and R. J. Nicholas, Carbon **43**, 1151 (2005)

48. M. F. Islam, D. E. Milkie, O. N. Torrens, A. G. Yodh, and J. M. Kikkawa, Phys. Rev. B **71**, 201401(R) (2005).

49. Y. Kim, and D. E. Luzzi, J. Phys. Chem. B **109**, 16636 (2005).

CHAPTER 2.

BASIC THEORETICAL CONCEPTS

2.1 SINGLE WALL CARBON NANOTUBES (SWNTs)

2.1.1 ELECTRONIC PROPERTIES OF SWNTs

SWNTs are formed by rolling a graphene layer as shown in figure 2.1.(a) [1,2]. Various physical properties of SWNTs are decided depending on which geometry they are rolled with, expressed by chiral vector $\vec{C_h}$,

$$\vec{C_h} = n\vec{a_1} + m\vec{a_2} \tag{2.1}$$

where $\vec{a_1}$ and $\vec{a_2}$ are unit vectors in a hexagonal lattice, and n, m are integers. When n is equal to m, a graphene layer is rolled up to be an "armchair" tube, which has an armchair-shaped end, as shown in the top of figure 2.1.(b). A zigzag tube is formed when m is zero as shown in the bottom of figure 2.1.(b), and all the other cases result in a chiral tube as shown in the middle of figure 2.1.(b).

(a)

(b)
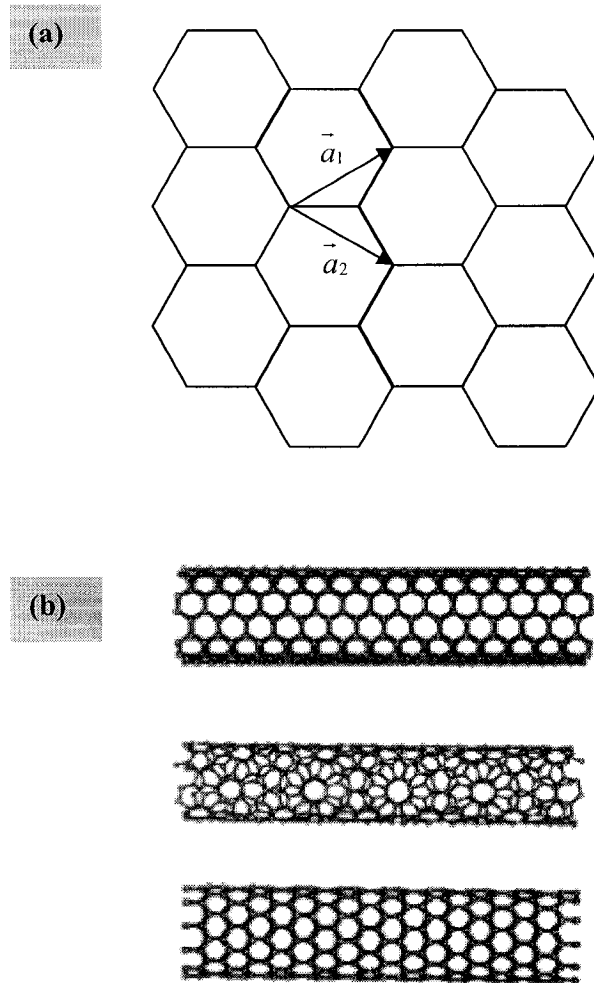
FIGURE 2.1 Structure of SWNTs. (a) A graphene layer showing hexagonal lattice with unit vectors $\vec{a_1}$ and $\vec{a_2}$. (b) A metallic (6,6) armchair nanotube (top), a semiconducting (8,3) chiral nanotube (middle), and a semiconducting (11,0) zigzag nanotube (bottom) [3].

With quasi one dimensional geometry, their electronic structures have unique van Hove singularity as shown in figure 2.2 [3,4]; the detailed derivation is described in Appendix A. As shown in the top curve, when *(n-m)* is an integer multiple of three, the electronic property of SWNTs is metallic with finite DOS at the Fermi level (as displayed with a circle in figure 2.2). If *(n-m)* is not an integer multiple of three, SWNTs have a semiconducting property due to zero DOS at the Fermi energy, as shown in the middle and bottom curves. In random sample distribution, therefore, one third of SWNTs are metallic and two third are semiconducting.
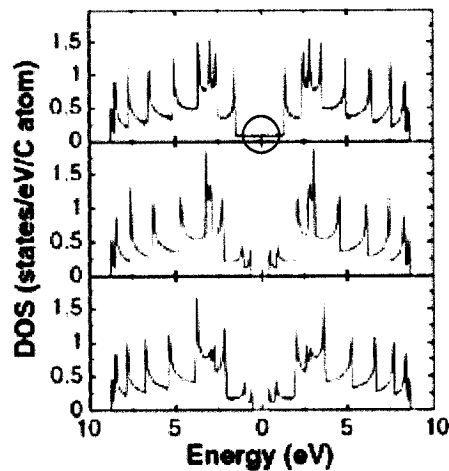
FIGURE 2.2 Density of states (DOS) for SWNTs displayed in figure 2.1 (b) [3]. A (6,6) metallic tube has a finite DOS at the Fermi energy as indicated by the circle at the top curve, while semiconducting tubes show zero DOS at the Fermi energy, as shown in two curves at the bottom.

2.1.2 OPTICAL PROPERTIES OF SWNTs

When light irradiates individual SWNTs, electronic absorption and subsequent emission happens. The schematic of the absorption and emission across the van Hove singularities is shown in figure 2. 3 [5,6]. For example, E_{22} absorption indicates the electronic transition from the second valence band, v_2, to the second conduction band, c_2, in semiconducting nanotubes [5]. The subsequent fluorescence, E_{11}, is then followed, which is the relaxation from the first conduction band, c_1, to the first valence band, v_1. Since the magnitude of the transitions depends on the electronic structure of nanotubes, absorption spectroscopy and fluorescence spectroscopy could be efficient characterization techniques to determine the composition of a bulk SWNT sample, such as diameter or chirality.
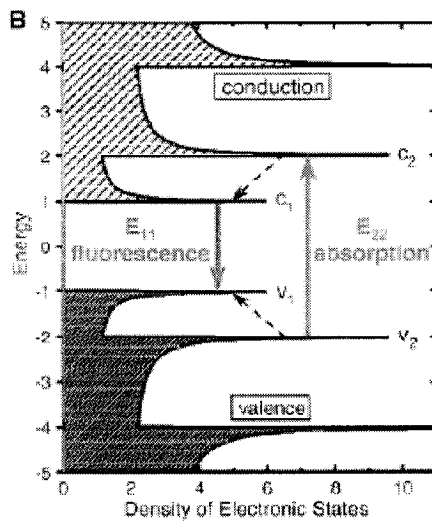
FIGURE 2.3 Optical electronic transition in a semiconducting SWNT. E_{22}, from the second valence band to the second conduction band, followed by emission, E_{11}, from the first conduction band to the first valence band [5].

14

2.1.3 VIBRATIONAL PROPERTIES OF SWNTs

When a sample is irradiated by light, most of the incident photons are scattered elastically. However, a small amount of them, one off 10^7 photons, are scattered inelastically and can provide the information of the vibrational modes (phonon) of a sample. As shown in figure 2. 4.(a), incident photons excite a sample from the ground state to a virtual state, and then inelastically scattered photons are emitted, leaving the sample in an excited vibrational state. This is called the Stokes Raman scattering. The opposite happens with smaller probability when a molecule is in an excited state already. In this case, inelastically scattered light has higher energy than that of incident light to relax the sample into the ground state. This is called anti-Stokes Raman scattering. In Raman measurement, the intensity of inelastically scattered lights is plotted as a function of the energy difference between incident lights and emitted lights, the so-called Raman shift, as shown in figure 2.4.(b).
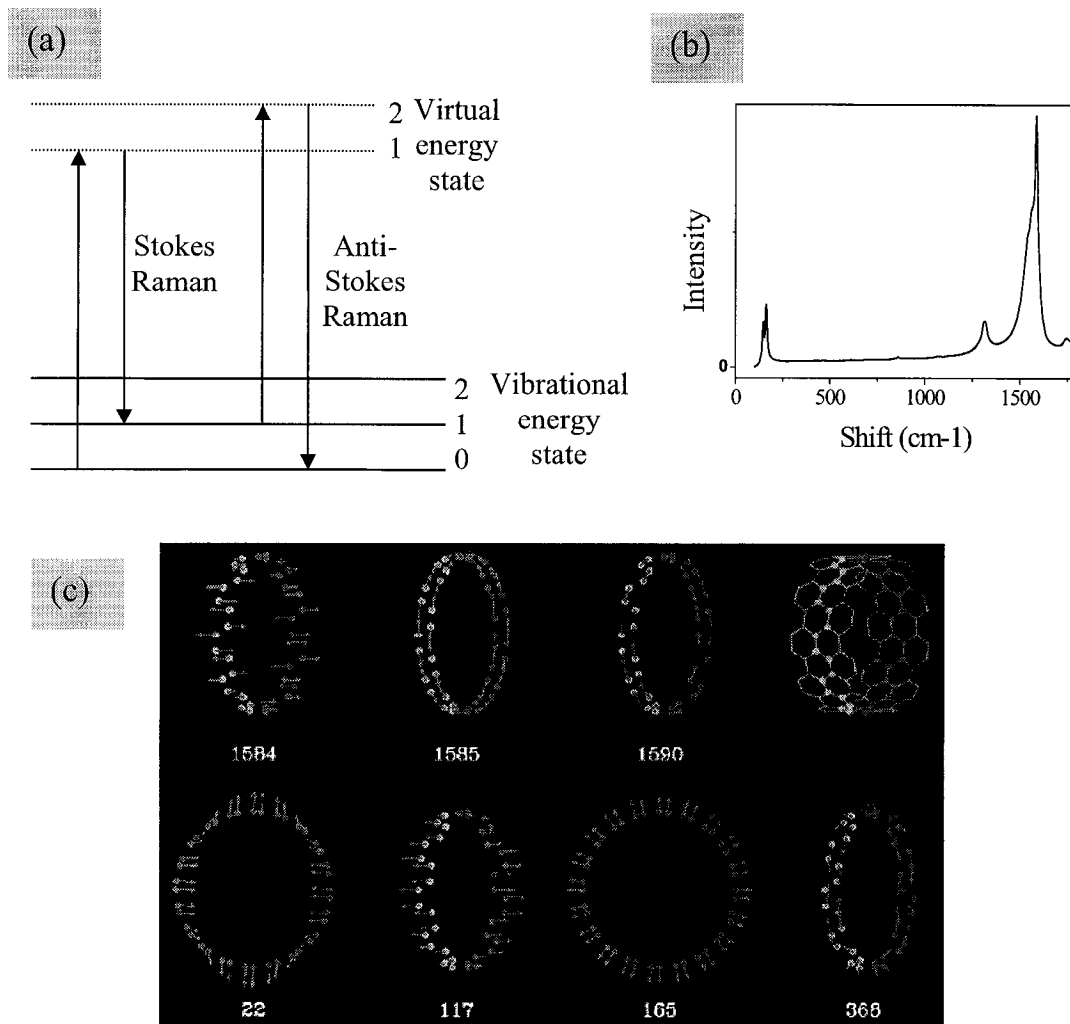
FIGURE 2.4 Raman spectroscopy and SWNT vibrational modes. (a) excitation from a ground state to a virtual state followed by the emission of inelastically scattered lights. While the inelastically scattered lights have less energy than that of incident lights in Stokes Raman, the former has greater energy than the latter in Anti-Stokes Raman. (b) Raman spectrum of SWNTs using 633 nm red laser. (c) Various Raman active modes in SWNTs. Tangential modes in the upper panel showing the movement of carbon atoms in plain, and radial breathing mode (RBM) in the lower panel showing the same displacement of carbon atoms in radial direction [7].

16

Figure 2. 4. (c) shows some of the Raman active modes of a (10, 10) nanotube [7]. As shown in the upper panel, tangential modes around 1580 cm^{-1} are the displacement of carbon atoms on the surface of nanotube, and hence it is present in graphite as well. What is unique in nanotubes is the radial breathing mode (RBM) around 200 cm^{-1}, as shown in the lower panel, where carbon atoms are moving in and out of the nanotube surface around the center with the same displacement.

RBM cannot be detected due to its weak intensity unless resonant Raman scattering takes place during a measurement [7]. When SWNTs undergo optical transition by an incident laser as shown in figure 2. 3., the excited electrons could enhance the RBM mode by as much as 10^6 times [8]. It should, therefore, be noticed that a different laser source in Raman would detect RBM of different diameter nanotubes whose electronic transition energy matches the energy of the incident laser.

The frequency of RBM (ω_{RBM}), is predicted to depend on the diameter of nanotubes, D, as given by the following equation,

$$D = \frac{\alpha}{\omega_{RBM}} \qquad (2.2)$$

where α is a constant (223.5 cm^{-1} nm [7] or 248 cm^{-1} nm [9]). Geometrically, the diameter of SWNTs can be calculated from chiral indices (n and m) as given by the following equation,

$$D = \frac{a}{\pi}\sqrt{n^2 + m^2 + nm} \qquad (2.3)$$

The exact diameter or charalities in a given sample can be efficiently obtained by using Raman spectroscopy combined with optical spectroscopy [7, 9].

2.1.4 MAGNETIC PROPERTIES OF SWNTs

An isolated carbon atom has an electron configuration of $1s^2\ 2s^2\ 2p^2$ as shown in

figure 2. 5. (a) [10]. Hybridization occurs due to the close energy levels between the $2s$

and $2p$ orbitals. A diamond structure is formed by four sp^3 orbitals to make tetrahedral

bonding as shown in figure 2. 5.(b). Graphite is formed by three sp^2 orbitals and a $2p$

orbital as shown in figure 2. 5.(c). The π electrons in the $2p$ orbital are known to induce a

ring current under a magnetic field, resulting in a huge diamagnetic property in graphite.
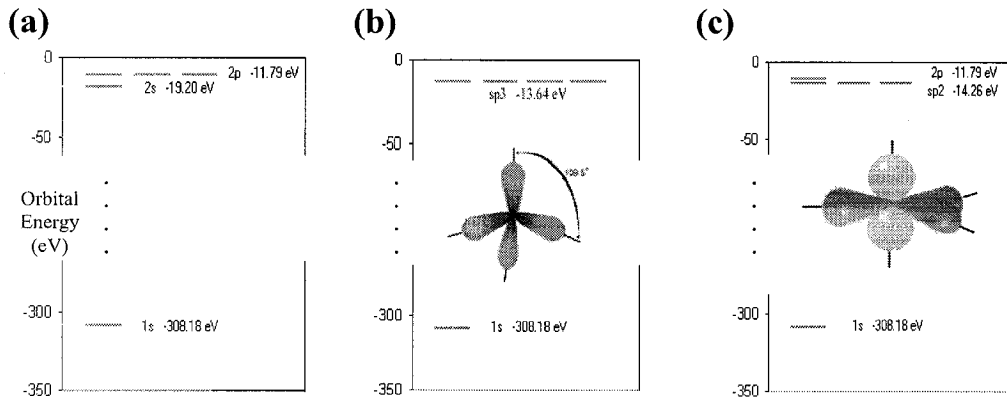
FIGURE 2.5 Various orbital structures of carbon atoms [10]. (a) an isolated carbon atom shows one $2s$ and three $2p$ orbitals (b) one $2s$ and three $2p$ orbitals are hybridized to make four sp^3 orbitals with a tetrahedral structure (c) one $2s$ and two $2p$ orbitals are hybridized to make three sp^2 orbitals. The other $2p$ orbital remains intact with a lone electron. (Note that the y-axis in the middle is chopped off.)

SWNTs have shown similar but not identical magnetic properties to those of

graphite [11-14]. Semiconducting nanotubes were predicted to show comparable

diamagnetic property to graphite in both perpendicular and parallel configuration with an

18

applied magnetic field. However, metallic nanotubes were expected to show a weak paramagnetic property in parallel configuration and a diamagnetic property in a perpendicular configuration. On average, the magnetic susceptibility of non-doped nanotubes with a 10 nm radius in random orientation was calculated to be -150×10^{-6} cgs/mole at room temperature [11].

The magnitude of ring current, which is responsible for the strong diamagnetic property of graphite and nanotubes, was measured using nanotube quantum dots (CNTQDs) [15]. As shown in figure 2. 6.(a), graphene is a zero energy gap semiconductor whose cone-shaped valence band meets conduction band at K points. When it is rolled to make a nanotube, the electron wavevector in radial direction, $\kappa_\perp$ is quantized due to quantum confinement, resulting in energy gap, E_g^0, in the case of a semiconducting nanotube as shown in figure 2. 6 (b) [16].

When a magnetic field is applied parallel to the nanotube axis, the energy will be split into two levels where the Zeeman splitting, ΔE, is equal to $-\vec{\mu} \cdot \vec{B}$. In CNTQD, energy levels of the conduction band under the magnetic field are then given by,

$$E = \frac{E_g^0}{2} + \frac{\hbar^2 \pi^2}{2m_i^* L^2} n^2 \pm \frac{\mu_{orb} B_{\parallel}}{2} \tag{2.4}$$

where the quantum number n is an integer, m_i^* is the effective mass, and L is the length of nanotubes.
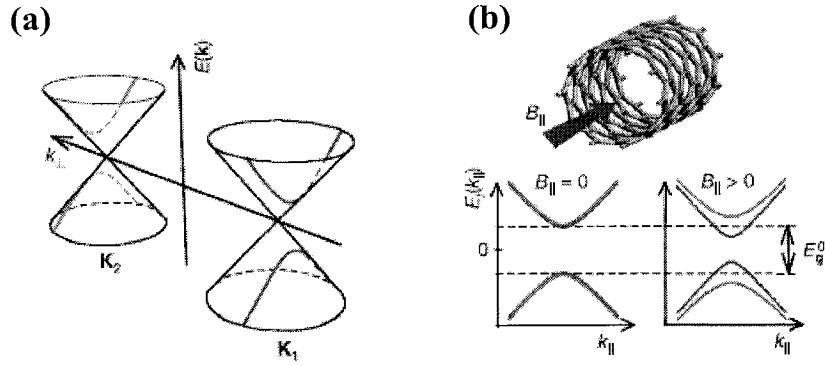
FIGURE 2.6 Zeeman splitting in a SWNT. (a) In a graphene layer, a cone-shaped conduction band meets a valence band at K_1 and K_2. When it is wrapped into a nanotube, $k_\perp$ is quantized due to quantum confinement, leading to an energy gap, E_g^0, in semiconducting nanotubes [15]. (b) The energy gap changes with an applied magnetic field due to the Zeeman splitting [15].

From the measurement of I/V_{sd}, the orbital magnetic moment, μ_{orb}, for a 2.6 *nm* diameter nanotube was obtained to be 0.7 ± 0.1 meVT^{-1}, which is ~ 15 times larger than the Bohr magneton in CNTs [17]. Such a large orbital magnetic moment justifies the existence of the ring current in SWNTs.

The local magnetic properties of SWNTs can be studied by NMR. In principle, different magnetic susceptibilities of semiconducting, metallic, or any given chirality SWNTs would result in distinct NMR peaks [18-22]. From the *ab-initio* calculation of the magnetic susceptibilities of (8,0) and (16,0) semiconducting nanotubes, the isotropic chemical shift is inferred to be 132 ppm and 124 ppm, respectively [22]. The bigger diameter nanotubes produce the larger diamagnetic shift due to the larger ring current.

20

The magnetic screening effect of SWNTs was also predicted in (8,0) @ (16,0) DWNTs [22]. When a magnetic field, B_0, is applied parallel to the nanotube axis, z, the induced current, j, on a nanotube surface can be expressed as,

$$j = \beta_\| B_0 \hat{\theta} \tag{2.5}$$

where, $\beta_\|$ is a constant and $\hat{\theta}$ is the unit vector along the azimuthal direction. The magnetization per unit length is then given by,

$$M = \frac{1}{2cL} \int d^3 r \vec{r} \times \vec{j}(r) = \frac{\beta_\| B_0}{c} \frac{\pi D^2}{4} \hat{z} \tag{2.6}$$

where c is the speed of light, L is the lattice parameter in the periodic direction, D is the diameter of a nanotube, and $\hat{z}$ is the z-direction unit vector (refer to Appendix B for a detailed description).

Magnetization can also be calculated using magnetic susceptibility, χ, as in the following equation,

$$M = \frac{\pi D}{N_A} n_C \chi_\| B_0 \tag{2.7}$$

where N_A is the Avogadro constant, and n_C is the density of carbon atoms in unit area. From the equations (2.6) and (2.7), the constant $\beta_\|$ is given by,

$$\beta_\| = c \frac{4 n_C}{N_A D} \chi_\| \tag{2.8}$$

From *Biot-Savart* law, a diamagnetic shift inside a nanotube due to the induced current is given by

$$\frac{B_{induced}}{B_0} = \frac{B_{inside} - B_0}{B_0} = 4\pi \frac{4n_C}{N_A D} \chi_\parallel \qquad (2.9)$$

The magnitude of an induced current on SWNTs is anisotropic since their magnetic susceptibility is anisotropic [23]. When an applied magnetic field is perpendicular to the nanotube axis, the induced current is $j = \pm \beta_\perp B_0 \hat{x}$, and the diamagnetic shift can be expressed as,

$$\frac{B_{induced}}{B_0} = \frac{B_{inside} - B_0}{B_0} = 4\pi \frac{2n_C}{N_A D} \chi_\perp \qquad (2.10)$$

From the magnetic susceptibility values obtained using *ab-initio* calculation, the diamagnetic shifts that a (8,0) nanotube feels inside a (16,0) nanotube were calculated to be − 24 and − 31 ppm in parallel and perpendicular configurations respectively. The resultant isotropic diamagnetic shift was -29 ppm, which was consistent with the value, 21 ppm, from their *ab-initio* calculation.

2.2 NUCLEAR MAGNETIC RESONANCE (NMR)

2.2.1 SPIN PRECESSION IN MANGETIC FIELD

The magnetic moment associated with an orbiting electron is defined as

$$\vec{\mu} = \gamma \vec{L} \qquad (2.11)$$

where $\vec{L}$ is angular momentum of the electron and γ is gyromagnetic ratio. As shown in figure 2. 7, an atom in a magnetic field, $\vec{B}$, has the energy, E, given by

$$E = -\vec{\mu} \cdot \vec{B} = \mu B \cos \theta \qquad (2.12)$$
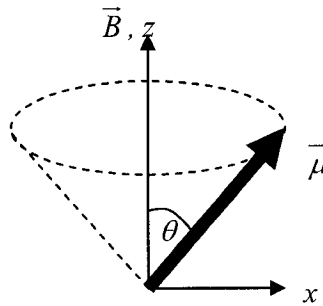
FIGURE 2.7 Nuclear spin precession under an external magnetic field, $\vec{B}$ [24].

A torque $\vec{G}$ is created under the magnetic field, $\vec{B}$, due to the angular momentum that the magnetic moment has,

$$\vec{G} = \vec{\mu} \times \vec{B} \qquad (2.13)$$

Since the torque is equal to the rate of the angular momentum change, the equation 2. 13 can be written as,

$$\frac{d\mu}{dt} = \gamma \vec{\mu} \times \vec{B}$$ (2.14)

The change in the magnetic moment, therefore, tends to be perpendicular to the magnetic moment and to the applied magnetic field as well. The spin is precessing around the applied magnetic field with the Larmor frequency, ω_L, given by,

$$\omega_L = \gamma B$$ (2.15)

The energy of a nucleus in a magnetic field, B_o, applied into the z direction is given by,

$$E = -\vec{\mu} \cdot \vec{B_0} = -g_N \mu_N I B_0 \qquad (2.16)$$

where g_N is the nuclear g-factor, μ_N is the nuclear magneton, and I is the nuclear spin quantum number. It has minimum energy when its magnetic moment is parallel to the magnetic field, whereas it has maximum energy when it is anti-parallel to the field. For a spin -1/2, the energy splitting of $g_N \mu_N B_0$, so-called Zeeman splitting, is produced as shown in figure 2. 8.
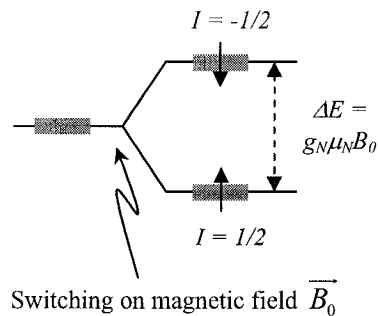
FIGURE 2.8 The Zeeman splitting under an external magnetic field, $\vec{B_0}$ [24].

At 0 K, all nuclear spins would take a low energy state. As the temperature increases, thermal fluctuations will perturb the population in those energy levels, and the final equilibrium population will be decided by the Boltzmann probability expression. For example, the Zeeman splitting for a proton is only $\sim 10^{-7}$ eV when a laboratory-scale

magnetic field of 1 Tesla is applied, whereas the thermal energy at room temperature is ~

10^{-2} eV. It is not possible, therefore, to detect such a tiny alignment at room temperature

unless the resonance technique is applied as explained in the following.

A sample is placed under the magnetic field $\overrightarrow{B_0}$ applied to the z axis, as shown in

figure 2. 9. Magnetic moments in the sample start to precess along the z axis with the

Larmor frequency, $\omega_L = \gamma B_0$. Despite the thermal perturbation, the overall magnetic

moment in the sample will be directed to the z axis, while the overall magnetic moments

in the x-y plane is zero due to random-isotropic precession.

Static $\overrightarrow{B_0}$

z

x

Sample in
RF coil

$\overrightarrow{B_1}$
oscillating
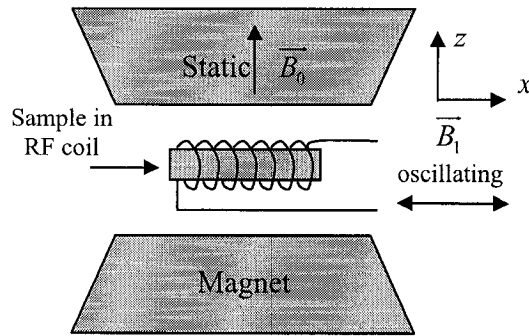
Magnet

FIGURE 2.9 The schematic diagram of NMR spectroscopy. The static
magnetic field $\overrightarrow{B_0}$ creates a total magnetic moment in a sample aligned to
the z-direction. The oscillating magnetic field $\overrightarrow{B_1}$, which is resonant with
the precession of nuclear spins in the sample, perturbs the moment to the x
or $-z$ direction depending on the types of measurements [24].

Now, the radio frequency (RF) pulse, $\vec{B_1}$, close to the Larmor frequency is applied to the x axis through the solenoid coil. Despite the tiny magnitude, the correctly-tuned frequency can rotate the overall magnetic moment from the z-axis (the dotted black arrow in figure 2. 10) to the x-axis (the solid black arrow in figure 2. 10). Once the RF pulse is turned off, the rotated magnetic moment starts to precess while being relaxed to the thermal equilibrium state (the dotted red arrow in figure 2. 10).
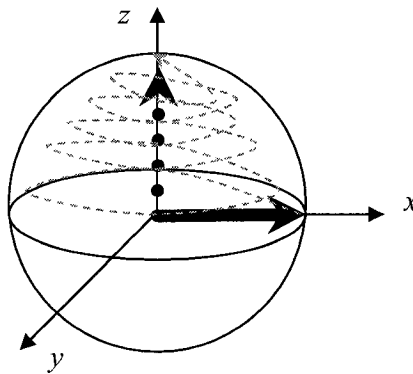
FIGURE 2.10 Relaxation of a magnetic moment. The perturbed magnetic moment in x-direction (solid black arrow) is precessing while being relaxed to the thermal equilibrium (dotted black arrow). The red dotted line represents the trace of the precession of the solid arrow [25].

The x component of the relaxation precession is detected by the solenoid coil to produce free induction decay (FID) as shown in figure 2. 11. (a). A nuclear spin is relaxed through interaction with neighboring spins which have slightly different Larmor frequencies. If there were no difference in the Larmor frequencies between them, the spins can precess forever in the x-y plane. Therefore, a FID is a superposition of several

FIDs corresponding to spins in different chemical environments. The Fourier transformation, finally, will transform the time scale in FID into the frequency scale in the usual NMR spectra. Nuclear spins in different chemical environments can be visualized by separate peaks as shown in figure 2. 11. (b).

(a)

amplitude

F. T.

(b)

intensity

0

200   150   100   5(

chemical shift (ppm)
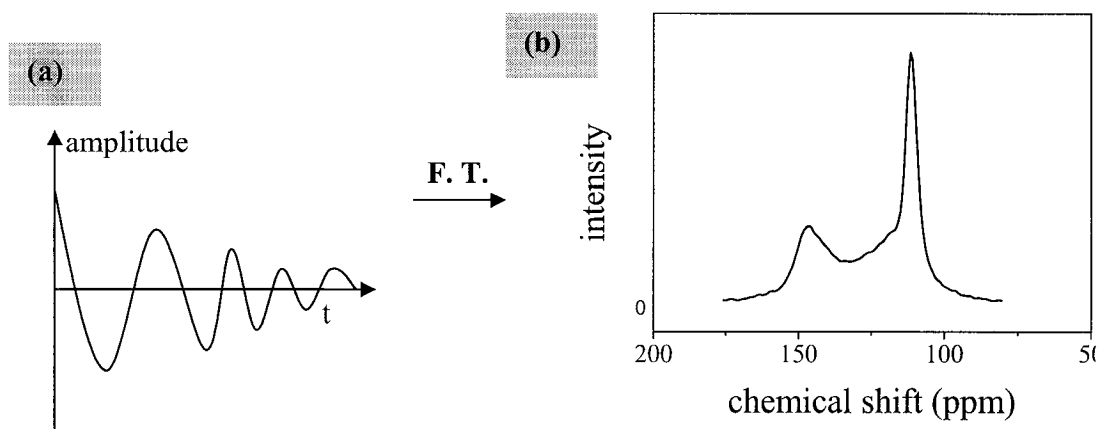
FIGURE 2.11 Free induction decay of NMR signal. (a) Free induction decay showing the x component of the magnetic moment during relaxation [25]. (b) Fourier transformation of the FID showing several different precession frequencies.

2.2.3 CHEMICAL SHIFT

The magnitude of a local magnetic field varies with that of an applied magnetic field. Therefore, it is convenient to express chemical shift, δ, by comparing the Larmor frequency of the atom of interest to that of a reference atom, as shown in the equation (2.17),

$$\delta = \frac{\omega_L - \omega_L^{Ref.}}{\omega_L^{Ref.}} \qquad (2.17)$$

28

where ω_L is the Larmor frequency of an isotope in the site of interest in a sample and ω_L^{Ref} is that of the same isotope in the reference sample under the same magnetic field. Usually tetramethylsilane is used as a reference sample for ^{13}C.

The chemical shift is very small, just a few ppm in the proton case, meaning that the local magnetic field is different from an applied magnetic field by only 10^{-6} times. Therefore, a uniform magnetic field throughout a sample is critical in NMR measurement to get a well-resolved signal. In the sense, conventionally purified SWNTs would not be appropriate because they still possess a substantial amount of ferromagnetic catalyst particles, which will destroy the uniform magnetic field in a sample.

Since the local magnetic field at a site of interest depends on the direction of the molecules relative to an applied magnetic field, the chemical shift raised from the local magnetic field has tensor property given by,

$$\delta = \begin{pmatrix} \delta_{xx} & \delta_{xy} & \delta_{xz} \\ \delta_{yx} & \delta_{yy} & \delta_{yz} \\ \delta_{zx} & \delta_{zy} & \delta_{zz} \end{pmatrix} \tag{2.18}$$

As non-secular terms is ignored at a high external magnetic field, the motion averaged chemical shift in an isotropic liquid is expressed as,

$$\delta_{iso} = \frac{1}{3}\left(\delta_{xx} + \delta_{yy} + \delta_{zz}\right) \tag{2.19}$$

Refer to Appendix C for the detailed derivation.

29

2.2.4 MAGIC ANGLE SPINNING (MAS)

In addition to the chemical shift caused by the chemical environment, the direct

dipole-dipole coupling (DD coupling) between nuclear spins affects local magnetic fields

significantly, as shown in figure 2. 12.
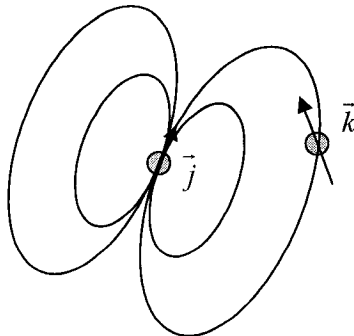
FIGURE 2.12 Dipole-dipole coupling. The magnetic field generated by
the nuclear spin $\vec{j}$ interacts with the spin $\vec{k}$ [25].

The Hamiltonian of DD coupling between spin $\vec{I_j}$ and $\vec{I_k}$ is represented by the following

equation,

$$\hat{H}_{jk}^{DD} = b_{jk}\left(3(\hat{I}_j \cdot \vec{e}_{jk})(\hat{I}_k \cdot \vec{e}_{jk}) - \vec{I_j} \cdot \vec{I_k}\right) \tag{2.20}$$

where $\vec{e}_{jk}$ is the unit vector of the line connecting the two nuclei. The DD coupling

constant, b_{jk}, is given by,

$$b_{jk} = -\frac{\mu_0}{4\pi}\frac{\gamma_j\gamma_k\hbar}{r_{jk}^3} \tag{2.21}$$

where γ_j and γ_k are the gyromagnetic ratio of the nuclear $\overrightarrow{I_j}$ and $\overrightarrow{I_k}$, respectively, and r_{jk} is the distance between the two spins.

In many spin systems, total DD coupling can be expressed as,

$$\widehat{H}^{DD} = \sum_{j<k} \widehat{H}_{jk}^{DD} \qquad (2.22)$$

Since the non-secular part of the DD coupling terms can be ignored in a high magnetic field, the total DD coupling in a homonuclear case is given,

$$\widehat{H}_{jk}^{DD}(\Theta_{jk}) = d_{jk}\left(3\hat{I}_{jz}\hat{I}_{kz} - \overrightarrow{I_j}\cdot\overrightarrow{I_k}\right) \qquad (2.23)$$

where the secular DD coupling, is expressed by,

$$d_{jk} = b_{jk}\frac{1}{2}\left(3\cos^2\Theta_{jk} - 1\right) \qquad (2.24)$$

where Θ_{jk} is the angle between the vector connecting the spins and the applied magnetic field as shown in figure 2. 13.
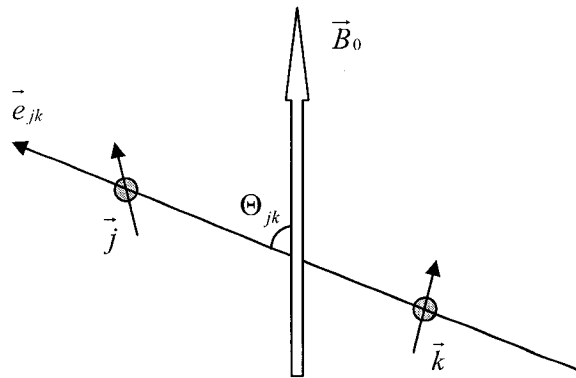
FIGURE 2.13 Secular DD coupling [25].

In an isotropic liquid, the DD coupling is averaged to zero because of the isotropic free rotation of spins, as being evaluated in the following calculation,

$$\int_0^\pi d\Theta_{jk} \sin\Theta_{jk} \left(3\cos^2\Theta_{jk} - 1\right) = 0 \qquad (2.25)$$

To the contrary, in a solid, DD coupling is non-zero because of the restriction of molecular motion. Complicated intra- and inter-molecular couplings will lead a broad signal not to be analyzed unless a magic angle spinning technique is employed. As shown in the equation 2.25, DD coupling will be zero when the angle Θ_{jk} is equal to $54.74°$, the so-called magic angle. By the mechanical rotation of the whole sample with the magic angle as shown in figure 2. 14, the molecules feel like they are isolated without DD coupling as in a liquid state, resulting in well-resolved signals.
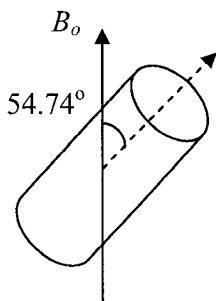
FIGURE. 2.14 Magic Angle Spinning (MAS). Mechanical spinning of a sample with the magic angle of $54.74°$ referenced to the applied magnetic field, B_0, cancels out all DD coupling.

2.2.5 RELAXATION PROCESS

2.2.5.1 TRANSVERSE RELAXATION (SPIN-SPIN RELAXATION)

Under the external magnetic field, B_0, applied in the z-axis, the overall magnetic moment in the sample will direct the z-axis with the Boltzmann distribution in the Zeeman splitting, as shown in figure 2. 15.(a). The absence of the coherency between nuclear spins results in no overall magnetic moment in the x and y components. Now, the application of a $\pi/2$ RF pulse makes the spin population in Zeeman energy levels even to remove the magnetic moment in the z-axis. Instead, the spins become coherent to have the total magnetic moment directed to the x-axis, as shown in figure 2. 15.(b).
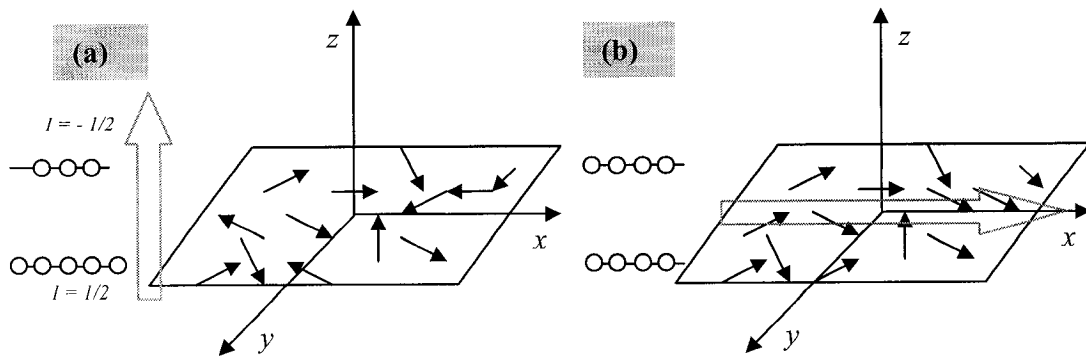
FIGURE 2.15 Perturbation of magnetic moments. (a) The thermal equilibrium state under the external magnetic field, B_0, applied to the z-direction. There is net magnetization in the z-direction (the red arrow) only, whereas there is no coherency in spin precession in the x-y plane [25]. (b) The RF pulse, B_1, which is resonant with the nuclear spin precession, perturbed the thermal equilibrium and created the spin coherency in the x-direction (the red arrow) at a certain time [25].

Once the RF pulse is turned off, the rotated magnetic moment starts to precess to return to the equilibrium state. The x component of the precession is detected by the solenoid coil, giving free induction decay (FID), as explained earlier. By fitting the envelope of FID using the following equation, the spin-spin relaxation time (T$_2$) can be obtained.

$$I(t) = I(0)e^{\frac{-t}{T_2}}$$
(2.26)

2.2.5.2. Longitudinal relaxation (spin-lattice relaxation)

The measurement of spin-lattice relaxation time, T$_1$, provides the valuable information on the dynamics and the motion of molecules. As shown in figure 2. 16, the application of a π pulse rotates the initial magnetic moment (the red arrow) to the $-z$ axis (the yellow arrow). Once the RF pulse is turned off, the magnetic moment is relaxed to the thermal equilibrium, following the equation

$$M(t) = M_0\left(1 - 2e^{\frac{-t}{T_1}}\right)$$
(2.27)

where M_0 is the saturated magnetic moment in thermal equilibrium. We need to measure the amplitude of the magnetic moment, $M(t)$, as a function of time, the so-called delay time. Since there will be no precession during the relaxation due to the absence of x-y magnetic components, a $\pi/2$ pulse is applied after a certain delay time to rotate the

moment (the blue arrow) into the x-y plane (the green arrow). M(t) can then be measured from the initial amplitude of FID.
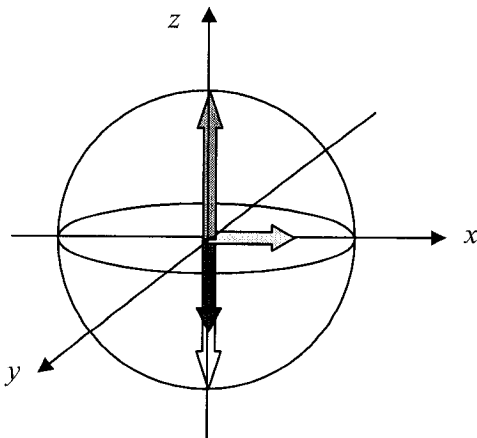
FIGURE 2.16 Spin-lattice relaxation time, T_1, measurement. The net magnetization in the thermal equilibrium (the red arrow) is perturbed into the $-z$ axis by an RF pulse (the yellow arrow). Once the pulse is turned off, the system starts to be relaxed into the thermal equilibrium without precession due to the absence of the x-y components in the magnetic moment. In a certain delay time, the partially relaxed moment (blue arrow) is rotated into the x-axis by the RF pulse (the green arrow) for its magnitude to be measured from the initial amplitude of the FID spectrum.

2.2.5.3 RANDOM FIELD RELAXATION

The nuclear spins are relaxed to a thermal equilibrium state when the local magnetic field, B_x, at the location of the spins keeps fluctuating (the so-called wobbling) due to the modulation of the dipolar field or a chemical shift by molecular rotation. In a simple model, the value of the transverse field, B_x, at a nuclear site can be plotted as a function of time as shown in figure 2. 17.
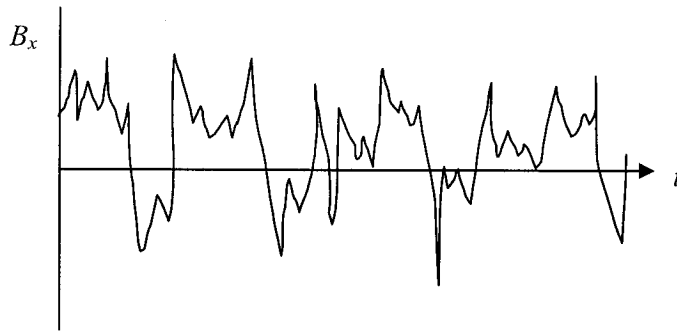
FIGURE 2.17 The fluctuation of the transverse field, B_x, due to molecular rotation. The average value $\langle B_x(t) \rangle$ is zero [25].

Relaxation depends on how large the fluctuation is as well as how fast the fluctuation is, which can be expressed by the autocorrelation function of the field given by,

$$G(\tau_c) = \langle B_x^2 \rangle e^{\frac{-\tau}{\tau_c}}$$

(2.28)

where $\left\langle B_x^2 \right\rangle$ is the mean square fluctuating field, and τ_c is the correlation time of the fluctuations. A smaller correlation time means faster fluctuation, which would result in faster relaxation.

Spectral density, $j(\omega)$, is then the Fourier transformation of the autocorrelation function expressed by,

$$J(\omega) = 2\int_0^\infty d\tau G(\tau)\exp\{-i\omega\tau\} \qquad (2.29)$$

Explicitly, the spectral density may be written as,

$$J(\omega) = 2\left\langle B_x^2 \right\rangle \frac{\tau_c}{1+\omega^2\tau_c^2} \qquad (2.30)$$

Finally, spin-lattice relaxation time can be expressed as,

$$T_1^{-1} = \gamma^2 \left\langle B_x^2 \right\rangle \frac{\tau_c}{1+(\omega_L\tau_c)^2} \qquad (2.31)$$

The usual trend of spin-lattice relaxation time is plotted as a function of correlation time in figure 2. 18. The most efficient relaxation occurs when the fluctuation speed of a local magnetic field matches the precession of a nuclear spin.

37
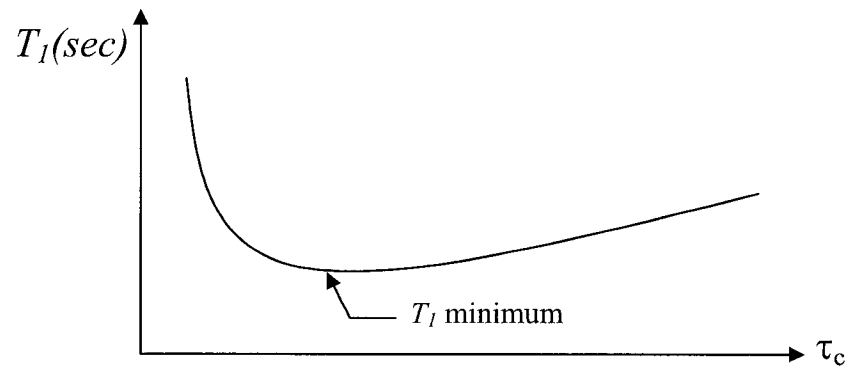
FIGURE 2.18 Spin-lattice relaxation time, T_1, as a function of autocorrelation time, τ_c. There is the minimum in T_1 at a certain autocorrelation time where the fluctuation of the local magnetic field due to the molecular rotation could be resonant with the spin precession, resulting in the efficient energy transfer of the spin to the lattice [25].

1. S. Iijima, and T. Ichihashi, Nature **363**, 603(1993).

2. R. Saito, M. Fujita, G. Dresselhaus, and M. S. Dresselhaus, Appl. Phys. Lett. **60**, 2204 (1992).

3. R. Saito, G. Dresselhaus, and M. S. Dresselhaus, *Physical Properties of Carbon Nanotubes*, Imperial College Press, London (1998).

4. L. Van Hove, Phys. Rev. **89**, 1189 (1953).

5. S. M. Bachilo, M. S. Strano, C. Kittrell, R. H. Hauge, R. E. Smalley, and R. Bruce Weisman, Science **298**, 2361(2002).

6. M. E. Itkis, S. Niyogi, M. E. Meng, M. A. Hamon, H. Hu, and R. C. Haddon, Nano. Lett. **2**, 155 (2002).

7. A. M. Rao, E. Richter, Shunji Bandow, Bruce Chase, P. C. Eklund, K. A. Williams, S. Fang, K. R. Subbaswamy, M. Menon, A. Thess, R. E. Smalley, G. Dresselhaus, and M. S. *Dresselhaus*, Science **275**, 187 (1997).

8. W. Hayes, and R. A. Loudon, *Light Scattering by Crystals*, Wiley, New York (1978).

9. A. Jorio, R. Saito, J.H. Hafner, C.M. Lieber, M. Hunter, T. Mcclure, G. Dresselhaus, and M.S. Dresselhaus, Phys. Rev. Lett. **86**, 1118 (2001).

10. http://invsee.asu.edu/nmodules/Carbonmod/bonding.html

11. J. P. Lu, Phys. Rev. Lett. **74** (7), 1123 (1995).

12. S. Zaric, G. N. Ostojic, J. Kono, J. Shaver, V. C. Moore, M. S. Strano, R. H. Hauge, R. E. Smalley, and X. Wei, Science **304**, 1129 (2004).

13. A. P. Ramirez, R. C. Haddon, O. Zhou, R. M. Fleming, J. Zhang, S. M. McClure, and R. E. Smalley, Science **265**, 84 (1994).

14. J. Heremans, C. H. Olk, and D. T. Morelli, Phys. Rev. B **49**, 15122 (1994).

15. E. D. Minot, Yuval Yaish, Vera Sazonova, and Paul L. McEuen, Nature **428**, 536 (2004).

16. L. L. Sohn, L. P. Kouwenhoven, and G. Schon, *Carbon Nanotubes*, Springer, New York, (2001).

39

17.   S. J. Tans, M. H. Devoret, R. J. A. Groeneveld, C. Dekker, Nature **394**, 761 (1998).

18.   X. P. Tang, A. Kleinhammes, H. Shimoda, L. Fleming, K. Y. Bennoune, S. Sinha, C. Bower, O. Zhou, and Y. Wu, Science **288**, 492 (2000).

19.   C. Goze-Bac, S. Latil, L. Vaccarini, P. Bernier, P. Gaveau, S. Tahir, V. Micholet, R. Aznar, A. Rubio, K. Metenier, and F. Beguin, Phys. Rev. B **63**, 100302 (2001).

20.   C. Goze-Bac, S. Latil, P. Lauginie, V. Jourdain, J. Conard, L. Duclaux, A. Rubio, and P. Bernier, Carbon **40**, 1825 (2002).

21.   N. A. Besley, J. J. Titman, and M. D. Wright, J. Am. Chem. Soc. **127**, 17948 (2005).

22.   M. A. L. Marques, M. d'Avezac, and F. Mauri, Phys. Rev. B **73**, 125433 (2006).

23.   O. N. Torrens, D. E. Milkie, H. Y. Ban, M. Zheng, G. Bibiana Onoa, T. D. Gierke, and J. M. Kikkawa, J. Am. Chem. Soc., **129** (2), 252 (2007).

24.   S. Blundell, *Magnetism in condensed matter*, Oxford University Press Inc., New York, (2001).

25.   M. H. Levitt, *Spin dynamics-basics of nuclear magnetic resonance*, John Wiley & Sons, LTD, New York, (2001).

26.   M. Mehring, *Princiles of high resolution NMR in solids*, Springer-Verlag, Berlin Heidelberg, New York, (1983).

CHAPTER 3

DEVELOPMENT OF NOVEL SWNT PURIFICATION

3.1 INTRODUCTION

Single wall carbon nanotubes (SWNTs) have generated significant interest due to their unique electrical, thermal, and mechanical properties [1-3]. These superior characteristics can be compromised in the presence of impurities, such as amorphous carbon or ferromagnetic catalyst particles, which are introduced during synthesis. For example, the electron spin resonance (ESR) signal is absent in catalyst-containing samples [4], and a similar effect is seen for nuclear magnetic resonance (NMR) where a broad line with about 1500ppm of anisotropy is observed for non purified SWNT materials [5, 6]. Measurement of the specific heat is obscured at low temperature because of nuclear hyperfine interactions in metallic impurities [7]. Small amounts of magnetic impurities can also influence nanotube electrical properties through Kondo-like interactions with conduction electrons [8, 9].

Various purification methods have been employed to remove magnetic impurities, such as chemical treatment, microwave heating, mechanical filtration, and heat treatment in a vacuum or oxidative environment [10-13]. However, a graphitic coating commonly found around ferromagnetic catalyst particles shields the particles from acid dissolution. Attempts to remove this graphitic coating often result in damage or destruction of SWNTs [13]. Although some groups applied magnetic filtration, the efficiency was low

such that ferromagnetism still dominated the magnetic moment of the sample for fields of order a few Tesla [14-17]. In order to circumvent this problem, other researchers synthesized nanotubes using non-ferromagnetic catalysts such as Rh/Pd or Rh/Pt [5,18]. While this enables an NMR investigation of the nanotubes, the thermal and electrical properties are still dominated by the metallic catalyst particles. Also, the small diameter (average of 0.85 nm) of these nanotubes renders them unsuitable for endohedral filling, which is an interesting way to functionalize nanotubes. By using isotopically-enriched ^{13}C, SWNT materials have been made from which NMR signals can be observed after magnetic processing using standard techniques common to biochemical fields [19]. These purification methods are insufficient to achieve the levels of purity necessary for electric and thermal applications and for the study of standard non-enriched nanotube materials. The high cost and low yield of SWNT materials provided by these methods make them ill-suited for mass production.

In this chapter, we present a new purification regimen that successfully removes ~ 99 % of ferromagnetic or superparamagnetic impurities, yielding diamagnetic nanotube samples, while also improving overall sample purity. Our method combines conventional air oxidation and chemical treatments with magnetic gradient filtration. In magnetic gradient filtration, a suspension containing the nanotubes is passed through a bed of iron beads in the presence of a 1.1 Tesla magnetic field. A locally inhomogeneous magnetic field, which is produced around the iron beads, is used to trap remnant magnetic impurities. Ferromagnetic catalyst particles, which have survived chemical purification due to the presence of a protective graphitic coating, are attracted to the iron beads with a

magnetic force $F = \nabla\left(\vec{\mu}\cdot\vec{B}\right)$, where $\vec{\mu}$ is the magnetic moment of the particle and $\vec{B}$ is the magnetic field whose local gradient is maximized by the iron beads. The method also works efficiently with suspensions of larger diameter SWNTs that can subsequently be filled with molecules to form high-purity, bulk 'peapod' materials.

3.2 ELECTROMAGNETIC FILTRATION SET-UP AND EXPERIMENTAL PROCESS

We obtained SWNT samples from Carbon Solutions (PII-SWNTs) produced by the electric arc discharge technique using a Ni/Y catalyst in a 4:1 % atomic ratio. As-received materials were already subjected to proprietary purification methods by the vendor and will heretofore be referred to as "pre-treated." Our purification procedure begins with oxidation in air at 560 °C for 10-30 min with a final yield of 40-60 wt. %. The resultant materials are then sonicated in concentrated hydrochloric acid (37.3%) at 60 °C for 40 min to dissolve bare catalyst particles, filtered through a 1.2 μm polycarbonate membrane, washed with distilled water, and dried at 100 °C for 5 min. Next, we create suspensions by adding 0.1-0.2 mg/ml N,N dimethylformamide (DMF), sonicating at 60 °C for 3-5 hrs.
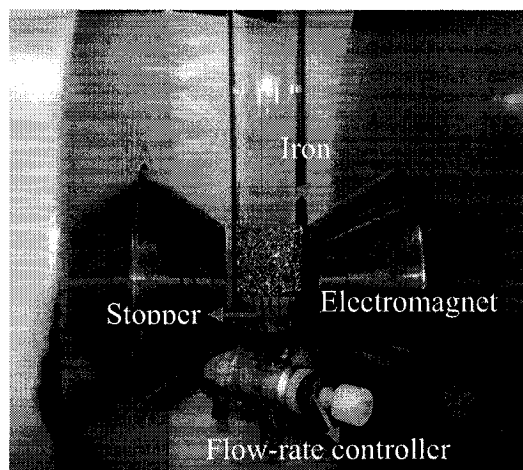
FIGURE 3.1 Schematic diagram of the magnetic gradient filtration setup

The dispersed SWNT solutions are filtered through a 1.1 Tesla magnetic gradient apparatus (Fig. 3.1) containing a 4 cm high filter bed of iron granules (99.98 % purity, 1-2 mm, Alfa Aesar). The solutions are passed through the apparatus 3 times at progressively slower rates (20 ml/min, 10 ml/min and 3 ml/min) while refreshing the iron granules after each cycle. Finally, suspensions are filtered through a $0.45 \mu m$ nylon membrane to recover the SWNTs, which are then annealed at 650 °C for 30 min in a dynamic vacuum ($\sim 2 \times 10^{-6}$ Torr) to remove residual DMF. We refer to the resulting samples as "purified". The instrumentation is laboratory scale; the purification starts with ~ 200 mg of pre-treated material and produces a final yield of 10-20 wt. %.

A variety of methods are used to measure the effect of our purification procedure on impurity content. Magnetometry probes the permanent moments associated with residual catalyst particles, and is performed in a Quantum Design Physical Property

44

Measurement System (PPMS). Thermogravimetric analysis (TGA), measures the total metal content (TA Instruments SDT 2960, ramp speed 10 °C/min at 70 sccm air flow), and the atomic constituents of the metal particles are identified using an Oxford energy dispersive X-ray spectrometer (EDS) on a scanning electron microscope (JEOL 6400). Estimation of the SWNT content in each sample is obtained using absorbance spectroscopy (Varian Cary 5000 UV-Vis-NIR Spectrophotometer) utilizing the rapid purity assessment method [20]. X-ray diffraction (XRD, copper K_α x-ray with wavelength $\lambda = 1.54$Å) is used to measure the relative increase of the SWNT bundle content due to purification by normalizing to the residual content of graphitic nanoparticles and multi-wall nanotubes. We also measure by XRD the fraction of bundled SWNTs that fill upon exposure to a vapor of C60 molecules, which is sensitive to surface cleanliness.

3.3 MAGNETIC PROPERTIES OF THE PURIFIED MATERIALS

Figure 3.2 shows a dramatic reduction in ferromagnetic impurity content upon purification. To ensure the accuracy of these data, we purified a large quantity of SWNTs so the diamagnetic moment of the sample can be accurately resolved above the diamagnetic background of the sample holder. The relative diamagnetic contribution of the holder was approximately 50 % that of the sample (Fig. 3.2a) and varied less than 2.5 % upon loading the holder ten times.
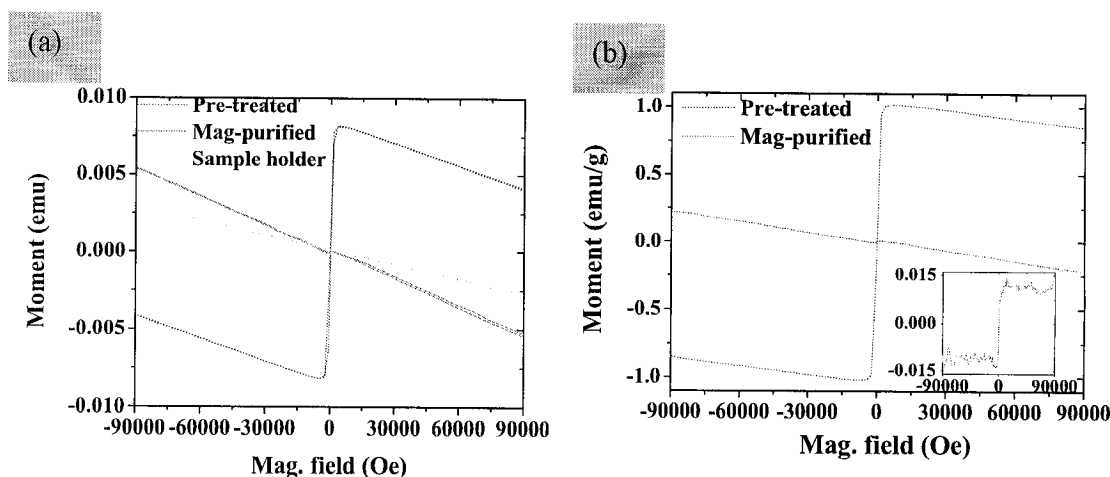
FIGURE 3.2 (a) Raw magnetic hysteresis loops of pre-treated SWNTs (8.18 mg, black line), magnetically purified SWNTs (11.56 mg, red line) and the empty sample holder (blue line). The Y-axis has units of raw emu, and is not divided by sample mass to explicitly reveal sample holder contributions to the raw data. (b) Mass-normalized magnetic moments of the pre-treated sample (black line) and the magnetically purified sample (red line). The inset shows the saturated permanent moment of the remaining catalyst particles in the mag-purified material obtained by subtracting the linear diamagnetic response at high magnetic fields. Magnetization data are taken at T = 300 K.

Figure 3.2b shows the mass-normalized magnetic moment after subtraction of the sample holder contribution from the raw data. The pre-treated sample is dominated by permanent moment contributions, whereas purified samples show a net diamagnetic response in fields exceeding 0.3 T. The saturation permanent moment is obtained by subtracting the high-field linear diamagnetic component from the mass-normalized magnetic moment as shown in the inset of Fig. 3.2b. Purification reduces this moment nearly two orders of magnitude from 1.04 emu/g to 0.013 emu/g. We find reasonable agreement with the latter when material from six separately purified samples is combined to form a larger sample, yielding a permanent moment of 0.012 emu/g.

3.4 OVERALL QUALITY OF THE PURIFIED MATERIALS

3.4.1 TRANSITION METAL CATALYST PARTICLES

We compare the overall purity of pre-treated and magnetically purified materials using TGA, EDS, absorption spectroscopy, and XRD. Metallic content is estimated from TGA assuming Ni and Y are oxidized to NiO and Y_2O_3 during TGA up to 1000 °C, and shows a reduction from 5-10 wt % in pre-treated materials to 1.3 % in purified samples. TGA residues are further weighed in an external microbalance to corroborate the TGA analysis. Because magnetic catalysts are metallic, it is surprising that metal content reduction during purification is within a single order of magnitude whereas the permanent moment is reduced by nearly two orders of magnitude. To understand this discrepancy,

TGA residues are evaluated by EDS. In each residue, two measurements are taken from separate areas, each measuring $\sim$2500μm^2, to ensure good statistics. Using internal standards, we find the Ni:Y ratio to be 20:1 in pre-treated samples. This result is somewhat surprising because the material originates from an arc-furnace with a cored graphite rod containing a 4:1 Ni:Y ratio. It is not clear whether the synthesis process or the subsequent purification regimen used by Carbon Solutions Inc. for their PII-SWNT product are the source of this Ni enrichment. In any event, we find that our purification procedure reduces the Ni:Y ratio from 20:1 to 2:1. This disproportionate reduction in Ni content during magnetic purification could explain the larger proportional reduction in permanent moment versus metallic content, as discussed below.

Magnetization studies confirm that magnetic gradient filtration effectively reduces ferromagnetic impurity content in SWNT material to 0.013 emu/g. We obtain a rough estimate of ferromagnetic metal content by initially assuming that the ferromagnetic component arises from Ni with a saturation moment of $\sim$50 emu/g (the value for bulk Ni) [21]. The corresponding ferromagnetic metal content is then $\sim$ 50 ppm, which is much smaller than the residual weight of the samples after carbon is removed during TGA measurements.

To understand this discrepancy, we note that TGA measures total metallic content, regardless of whether or not that material is ferromagnetic. Since PII-SWNTs are produced under conditions far from equilibrium, one may expect catalyst metallic composition will vary based on local conditions during synthesis and that deviations from the phase rule probably exist [22]. For the pre-treated sample, EDS shows that TGA

48

residues after heating in air to 1000 °C have a Ni:Y atomic ratio of 20:1. In such samples, one expects the majority of catalyst particles to be ferromagnetic [23]. In contrast, TGA residues from the magnetically purified materials contain lower Ni:Y ratios of 2:1. It is known that Y rich Y-Ni alloys show very weak itinerant ferromagnetism, or Pauli paramagnetism, depending on the Y content and temperature [24]; Ni_2Y, Ni_3Y, Ni_7Y_2, and Ni_5Y are all paramagnetic at room temperature. In the magnetically purified materials, it can be reasonably assumed that the composition of the nanoparticles varies over some range. Most of the particles with average or higher Y content would provide a paramagnetic contribution, while the small number of remaining Ni-rich particles would be weakly ferromagnetic consistent with the data.

3.4.2 SWNT CONTENT IN PURIFIED SAMPLES

Although developed for magnetic purification, our procedure also improves other benchmarks of sample purity and quality. Optical absorbance shows an improvement in SWNT abundance, XRD shows enhanced crystallinity indicating improved SWNT content, filling experiments show efficient formation of peapod structures indicating clean SWNT surfaces, and ^{13}C MAS-NMR confirms the absence of the ferromagnetic catalyst particles as well as the pre-dominance of the clean SWNTs in purified materials.

Optical absorbance shows that our new purification method increases SWNT content relative to other carbonaceous species. For these studies, samples are annealed at 900 °C for 5 hrs in vacuum to heal defects which can influence the absorbance spectrum

49

[17]. Samples are then sonicated in DMF for 3 hr to a concentration of 0.01 mg/ml. Following the rapid SWNT-purity assessment method of Landi, et al [20], we obtain the ratio of absorbance values for the peak maxima of S_{22} and M_{11} bands, AS_{22}/AM_{11}, as indicated in Fig. 3.3(a) and substitute them into the empirical fitting equation for arc-SWNT in the paper. We find the absolute SWNT mass fraction in the carbonaceous material increases from 50 ± 7 % in the pre-treated sample to 71 ± 7 % in the magnetically purified sample. The measured increase in the nanotube content is consistent with the result from the relative evaluation method of Itkis, et al [25]. Using the integrated peak-to-background strength at the S_{22} peak, choosing spectral cutoffs at 0.96 and 1.46 eV, we find the peak-to-background ratio increases from 0.112 in the pre-treated material to 0.175 in the magnetically purified materials, which is a ~ 50 % increase in the relative nanotube content.
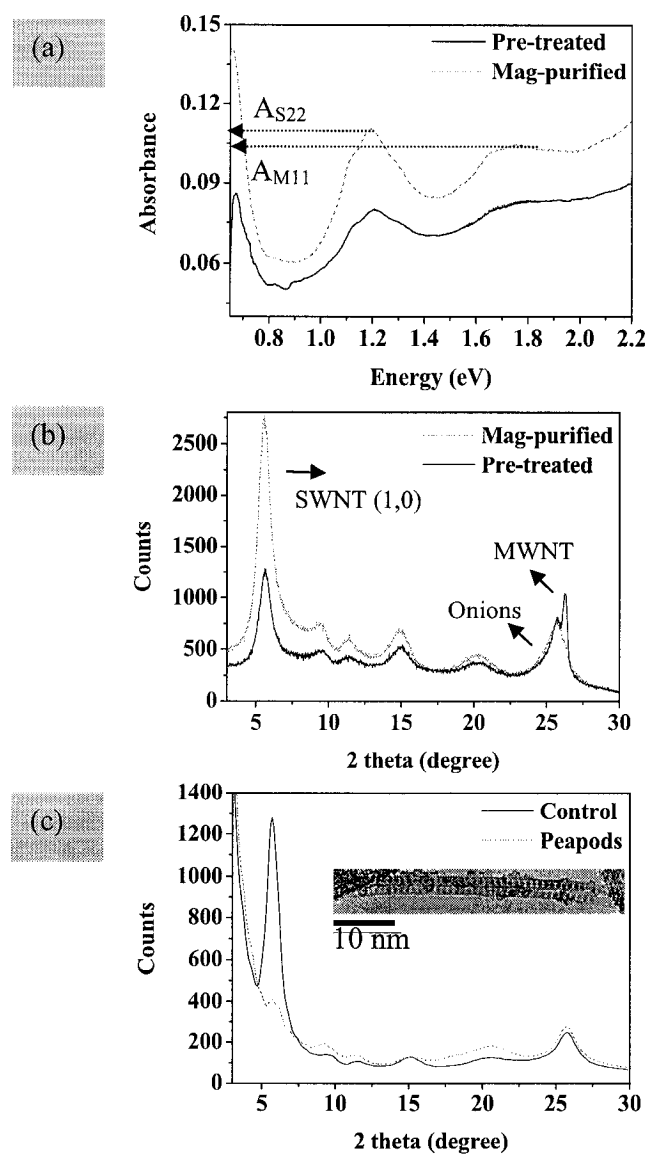
FIGURE 3.3 (a) The NIR absorption spectra for the SWNT-content estimation using the slopes between the peak maxima of S_{22} and $M_1 1$ bands. (b) XRD of the pre-treated (black line) and the magnetically purified samples (red line). (c) XRD patterns of the purified SWNT control sample and the peapod sample for evaluation of the C_{60} filling efficiency. Inset shows a typical TEM micrograph of the peapods.

In figure 3.3(b), buckypapers of pre-treated and purified material are compared by XRD. When normalized to the intensity of the graphitic onion peak ($2\theta = 25.6°$) [4], the intensity of the SWNT rope peak ($2\theta = 5.6°$) in the magnetically purified sample is 2.4 times greater after purification than the intensity of the same peak prior to purification. The sharp peak at $2\theta = 26.2°$, due to multi-wall nanotubes (MWNTs) is only present in the pre-treated spectrum indicating efficient removal during purification [26]. MWNTs, which tend to grow from large catalyst particles, would be easily attracted to iron granules during magnetic filtration. These XRD results indicate increased SWNT content relative to other graphitic carbon species, in accord with the optical absorbance data.

The filling of SWNTs with C_{60} fullerenes can provide a qualitative measure of SWNT cleanliness. Prior work has shown that efficient filling of carbon nanotubes requires open tubes and a clean surface [27]. Here, filling is accomplished by annealing at 650°C for 6 hrs under conditions previously reported [28]. In figure 3.3(c), XRD of powder samples shows a strong reduction in the intensity of the (10) SWNT rope peak ($2\theta = 5.6°$) after filling. This signal attenuation, which arises due to interference between the structure factor of the hexagonal lattice of SWNT bundles and the Bessel function of the form factor of C_{60}, can be used to calculate the fraction of filled nanotubes [29]. In the present case, we calculate a filling fraction of 95%. This high value indicates that the SWNTs in the material are clean, especially at open ends and large side-wall defects [26], and that the interior diameter of PII-SWNTs is sufficiently large to accommodate C_{60}. A

representative TEM micrograph of the peapod sample appears in the figure 3.3(c) inset, showing dense filling of SWNTs with C_{60}.

3.5 DETERMINATION OF THE DIAMAGNETIC SUSCEPTIBILITY OF SWNTs

With these purified samples we can also make some estimates of SWNT diamagnetic susceptibility, which may be compared with theory. From the slope of the magnetization curves the overall sample susceptibility is - 2.1 × 10^{-6} emu/g for pre-treated samples, and $(-2.9 \pm 0.42) \times 10^{-6}$ emu/g for magnetically purified samples at room temperature. Since it is impossible to accurately estimate the contents of MWNT and paramagnetic catalysts in the pre-treated material, which is a significant factor for the determination of the diamagnetic susceptibility of SWNT, we focus on the magnetically purified materials. From optical absorbance, we estimate SWNT content to be 71 ± 7 wt. % in magnetically purified materials. Carbon impurities in the magnetically purified material consist of amorphous carbon and graphitic onions as confirmed by XRD and TEM. The graphitic onion content was calculated to be 6 ± 1 wt. % from XRD, TGA, and TEM. The remaining content, 22 ± 7 wt. %, is most likely amorphous carbon. The susceptibilities of amorphous carbon and graphitic onion are approximately 0.2×10^{-6} and -2.1×10^{-6}, respectively [30, 31]. Pure Y has a paramagnetic susceptibility of 187 × 10^{-6} emu/g at room temperature [32]. Assuming 0.5 wt. % pure Y in the sample, this accounts for $\sim 1 \times 10^{-6}$ emu/g of the observed signal. Assuming that the purified material is composed of these four constituents, the resultant calculated susceptibility for SWNTs

is ~ -5 × 10^{-6} emu/g. Analytical theory shows the magnetic susceptibility of SWNTs scales with radius and is highly sensitive to carrier concentration due to Van Hove singularities in the band structure [34]. A zero-doping, zero-temperature, orientationally averaged estimate of SWNT diamagnetism for a mean diameter of 1.4 nm is ~ -0.64 × 10^{-6} emu/g. This value is well below our measurement, although temperature and doping can affect this theoretical estimate significantly.

3.6 CONCLUSIONS

Numerous spectroscopies such as ESR and NMR require highly pure SWNT samples. We describe a new purification method of single-wall carbon nanotube materials, air oxidation-hydrochloric acid treatment followed by magnetic filtration, which reduces the ferromagnetic catalyst content by nearly two orders of magnitude. Moreover, we find the new purification method significantly increases SWNT content relative to pre-treated materials, and yields clean surfaces suitable for filling experiments. Although the current yield is ~ 5 mg/hour due to the laboratory-scale experimental set-up, there should be no limiting factor for mass-production as long as large volume SWNT dispersions are stable and a sufficient magnetic field can be generated.

1. J. Vavro, J. M. Kikkawa, and J. E. Fischer, Phy. Rev. B **71**, 155410 (2005).

2. J. Hone, B. Batlogg, Z. Benes, A. T. Johnson, and J. E. Fischer, Science **289**, 1730 (2000).

3. P. Jaroenapibal, D. E. Luzzi, and S. Evoy, Appl. Phy. Lett. **85**, 4328 (2004).

4. A. S. Claye, N. M. Nemes, A. Janossy, and J. E. Fischer, Phys. Rev. B, **62**, R4845 (2000).

5. X. P. Tang, A. Kleinhammes, H. Shimoda, L. Fleming, K. Y. Bennoune, S. Sinha, C. Bower, O. Zhou, and Y. Wu, Science, **288**, 492 (2000).

6. C. Goze-Bac, S. Latil, L. Vaccarini, P. Bernier, P. Gaveau, S. Tahir, V. Micholet, R. Aznar, A. Rubio, K. Metenier, and F. Beguin, Phys. Rev. B, **63**, 100302 (2001).

7. J. C. Lasjaunias, K. Biljakovic, Z. Benes, J. E. Fischer, and P. Monceau, Phy. Rev. B, **65**, 113409 (2002).

8. L. Grigorian, G. U. Sumanasekera, A. L. Loper, S. L. Fang, J. L. Allen, and P. C. Eklund, Phys. Rev. B, **60**, R11309 (1999).

9. R. S. Gracia, T. M. Nieuwenhuizen, and I. V. Lerner, Europhys. Lett., **66**, 419 (2004).

10. A. G. Rinzler, J. Liu, H. Dai, P. Nikolaev, C. B. Huffman, F. J. Rodriguez-Macias, P. J. Boul, A. H. Lu, D. Heymann, D. T. Colbert, R. S. Lee, J. E. Fischer, A. M. Rao, P. C. Eklund, and R. E. Smalley, App. Phy. A, **67**, 29 (1998).

11. K. L. Strong, D. P. Anderson, K. Lafdi, and J. N. Kuhn, Carbon, **41**, 1477 (2003).

12. A. R. Harutyunyan, B. K. Pradhan, J. Chang, G. Chen, and P. C. Eklund, J. Phys. Chem. B, **106**, 8671 (2002).

13. W. Zhou, Y. H. Ooi, R. Russo, P. Papanek, D. E. Luzzi, J. E. Fischer, M. J. Bronikowski, P. A. Willis, and R. E. Smalley, Chem. Phys. Lett, **350**, 6 (2001).

14. L. Thien-Nga, K. Hernadi, E. Ljubovic, S. Garaj, and L. Forro, Nano Lett., **2**, 1349 (2002).

15. J. G. Wiltshire, L. J. Li, A. N. Kholbystov, C. J. Padbury, G. A. D. Briggs, and R. J. Nicholas, Carbon, **43**, 1151 (2005).

16. M. F. Islam, D. E. Milkie, O. N. Torrens, A. G. Yodh, and J. M. Kikkawa, Phys. Rev. B, **71**, 201401(R) (2005).

17. Y. Kim, and D. E. Luzzi, J. Phys. Chem. B, **109**, 16636 (2005).

18. C. Goze-Bac, S. Latil, P. Lauginie, V. Jourdain, J. Conard, L. Duclaux, A. Rubio, and P. Bernier, Carbon, **40**, 1825 (2002).

19. A. Kitaygorodskiy, W. Wang, S-Y. Xie, Y. Lin, K. A. Shiral Fernando, X. Wang, L. Qu, B. Chen, and Y-P. Sun, J. Am. Chem. Soc., **127**, 7517 (2005).

20. B. J. Landi, H. J. Ruf, C. M. Evans, C. D. Cress, and R. P. Raffaelle, J. Phys. Chem. B, **109**, 9952 (2005).

21. I. M. L. Billas, A. Chatelain, and W. A. de Heer, Science, **265**, 1682 (1994).

22. M. Yudasaka, N. Sensui, M. Takizawa, S. Bandow, T. Ichihashi, and S. Iijima, Chem. Phys. Lett., **312**, 155 (1999).

23. A. Lienard, and J. P. Rebouillat, J. Appl. Phys., **49** (3), 1680 (1978).

24. D. Gignoux, R. Lemaire, P. Molho, and F. Tasset, J. Appl. Phys., **52**(3), 2087 (1981).

25. M. E. Itkis, D. E. Perea, S. Niyogi, S. M. Rickard, M. A. Hamon, H. Hu, B. Zhao, and R. C. Haddon, Nano Lett., **3**, 309 (2003).

26. O. Zhou, R. M. Fleming, D. W. Murphy, C. H. Chen, R. C. Haddon, A. P. Ramirez, and S. H. Glarum, Science, **263**, 1744 (1994).

27. B. W. Smith, and D. E. Luzzi, Chem. Phys. Lett., **321**, 169 (2000).

28. B. W. Smith, R. M. Russo, S. B. Chikkannanavar, and D. E. Luzzi, J. Appl. Phys., **91** (11), 9333 (2002).

29. H. Kataura, Y. Maniwa, M. Abe, A. Fujiwara, T. Kodama, K. Kikuchi, H. Imahori, Y. Misaki, S. Suzuki, and Y. Achiba, Appl. Phys. A, **74**, 349 (2002).

30. K. Takai, M. Oga, T. Enoki, and A. Taomoto, Diam. Relat. Mater., **13**, 1469 (2004).

31. O. E. Andersson, B. L. V. Prasad, H. Sato, T. Enoki, Y. Hishiyama, Y. Kaburagi, M. Yoshikawa, and S. Bandow, Phys. Rev. B, **58** (24), 16387 (1998).

32. W. E. Gardner, and J. Penfold, M. A. Taylor, Proc. Phys. Soc., **85**, 963 (1965).

33.	J. P. Lu, Phys. Rev. Lett., **74** (7), 1123 (1995).

CHAPTER 4

NUCLEAR MAGNETIC RESONANCE IN SWNTs

4.1. INTRODUCTION

Since the discovery of fullerenes by Kroto *et al.*, their electronic, optical and biological properties have been investigated extensively [1-8]. Interestingly, C_{60}, the rather large molecule, undergoes three different dynamic transitions with temperature [4-8]. From 300 K to 260 K, they show free rotation with the face centered cubic (FCC) structure. From 260 K to 100 K, they perform hindered rotation while changing their structure to simple cubic by orientational ordering [4]. In this region, single or double bonds face the centers of pentagons or hexagons to maximize Coulomb attraction [8]. The hindered rotation stops in the NMR time scale below around 100 K.

Among various properties of SWNTs [9-13], the quasi 1-D inner space they provide is unique, using which certain nano engineering with a material of interest can be performed. Peapods, being 1-D fullerene array inside SWNTs, are one good example such nano engineering [14,15]. The dynamics and phase transition of 1-D fullerenes are expected to be different from those in 3-D, due to the reduction in nearest neighbors from twelve in 3-D bulk to two in 1-D peapods [16]. The lower probability in 1-D chain system for a bond in a fullerene to find a center of a pentagon or a hexagon in a neighboring fullerene may lead to lower orientational ordering temperature. Also, charge

transfer from fullerenes into SWNTs may restrict their rotation even at room temperature [14].

In addition to the study of dynamics, 1-D fullerenes can be used as NMR probes to investigate the local magnetic properties of SWNTs. Marquis et al. predicted magnetic shielding of SWNTs due to the presence of ring current by the π electrons [17]. However, a few experimental NMR studies on encapsulated molecules in SWNTs showed no clear evidence of diamagnetic shielding, possibly due to the remaining ferromagnetic catalyst particles present in the samples [18-20].

In this chapter, we have investigated the 1-D dynamics of fullerenes and the local magnetic properties of SWNTs using NMR spectroscopy. The problem with the NMR signal being broadened in conventionally purified SWNTs is solved by the novel magnetic purification approach as elaborated in section 4.3 [21-22]. We have synthesized ^{13}C enriched peapods by introducing 25% ^{13}C enriched fullerenes into magnetically purified SWNTs and the analysis of their NMR spectra is described in section 4.4. Encapsulated 1-D fullerenes were found to undergo dynamic transition, similar to that in a bulk state, but with a much lower dynamic transition temperature, by as much as 160 K. A strong diamagnetic shielding by SWNT encapsulation has also been confirmed. In section 4.5, we present NMR data on DWNTs which were made through heat treatment of ^{13}C enriched peapods. Two separated well resolved NMR peaks are observed, one for diamagnetically shifted inner tubes and the other for paramagnetically shifted inner tubes. The electronic properties of ^{13}C enriched inner nanotubes are also investigated.

4.2 PREPARATION OF PEAPODs AND DWNTs

As-received PII-SWNTs purchased from Carbon Solutions Inc. were purified with the novel magnetic filtration method as described in chapter 3. The magnetically purified SWNT materials (~ 30 mg) and 25% ^{13}C enriched fullerenes purchased from MER Corporation (~ 20 mg) were outgassed in a dynamic vacuum of 10^{-6} Torr at 650°C and 300°C respectively, for an hour. The quartz tube containing the SWNTs and fullerene materials was sealed and annealed at 650°C for 10 hours in order for the fullerenes to fill the interiors of the SWNTs. After the filling step, the resulting peapod materials were post-annealed in a dynamic vacuum at 650°C for an hour to remove the non-encapsulated fullerenes. This sample meant for NMR studies is referred to as sample A.

For peapod sample B, PII-SWNTs from Carbon solution, Inc. were purified using conventional HNO_3 refluxing treatment. The process of peapod production is similar to that in sample A except the use of 16% ^{13}C enriched C_{60}. Samples of DWNTs were synthesized through the heat treatment of a batch of sample A at 1250 °C for 48 hrs under dynamic vacuum of 10^{-6} Torr.

X-ray diffraction (XRD, copper K_α with a wavelength of 1.54 Å) was used to assess the filling efficiency of the fullerenes into the SWNTs. The development of the inner tubes in DWNTs was verified using Renishaw 1000 Raman spectrometer operating with a red laser (wavelength, 633 nm). The samples of peapods and DWNTs were examined using a JOEL 2010 transmission electron microscope. ^{13}C NMR experiments were carried out using a Bruker ASX200 spectrometer at a magnetic field of 4.2 T and at

Larmor frequency of 50.3 MHz. The spin-lattice relaxation time was measured by a saturation-recovery technique. Temperature studies in NMR were performed in a sealed glass tube after being evacuated overnight at a dynamic vacuum of 10^{-8} Torr.

The magnetically purified SWNT materials, which have as low as 50 ppm of remnant ferromagnetic Ni-enriched catalyst particles and are diamagnetic, should be suitable for a number of experiments that have historically been difficult to conduct. Figure 4.1 shows the high resolution ^{13}C MAS NMR spectrum recorded on the magnetically purified powder. The isotropic chemical shift of the sp^2 carbon is observed at 118.8 ppm, referenced to TMS, which is in good agreement with previous experimental and theoretical values [23-26]. A reduction of the full width at half maximum of the isotropic line from typically 50 ppm, as observed in earlier studies [23-25] down to 18.80 ppm is consistent with a low content of magnetic impurities in our materials.
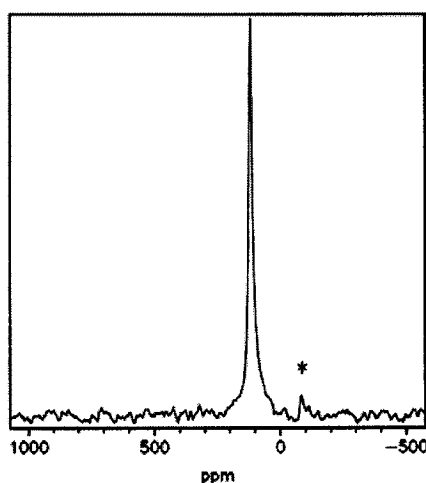
FIGURE 4.1 High resolution ^{13}C MAS NMR spectrum of the magnetically purified sample at room temperature. The limited number of sidebands (single) shows a chemical shift anisotropy typical for sp^2 carbon with no additional source of broadening, which is consistent with a high quality material [24].

4.3.2 SPIN-LATTICE RELAXATION STUDY AT ROOM TEMPERATURE

In figure 4.2, we show the magnetization recovery after saturation as a function of the relaxation delay at room temperature. Since the nuclear spin lattice relaxation time (T_1) of the carbon is sensitive to the presence of conduction electrons, a faster relaxation is expected for metallic nanotubes compared to semiconducting nanotubes [23,25]. Our data are consistent with a double exponential decay,

$$1 - \frac{M(t)}{M_0} = \alpha \exp\left(\frac{-t}{T_{1\alpha}}\right) + \beta \exp\left(\frac{-t}{T_{1\beta}}\right) \tag{4.1}$$

where $\alpha = 0.4$, $\beta = 0.6$, $T_{1\alpha} = 3$ sec and $T_{1\beta} = 31$ sec in metallic and semiconducting SWNTs, respectively.
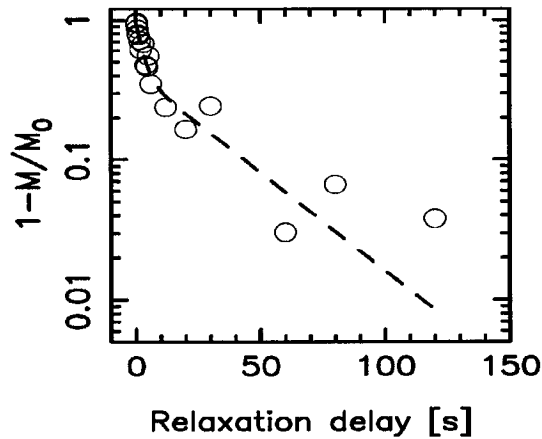
FIGURE 4.2 Magnetization recovery of the magnetically purified SWNTs as a function of relaxation delay at room temperature.

4.4.1 ^{13}C MAS NMR

4.4.1.1 DIAMAGNETIC SHIFT OF ENCAPSULATED FULLERENES

Figure 4.3 shows ^{13}C-MAS NMR spectra of peapods along with magnetically purified SWNTs for comparison. Despite non-enriched natural carbon, the purified SWNTs produce a well-resolved NMR peak at 118.8 ppm with FWHM of 18.80 ppm as shown in figure 4. 3(a).
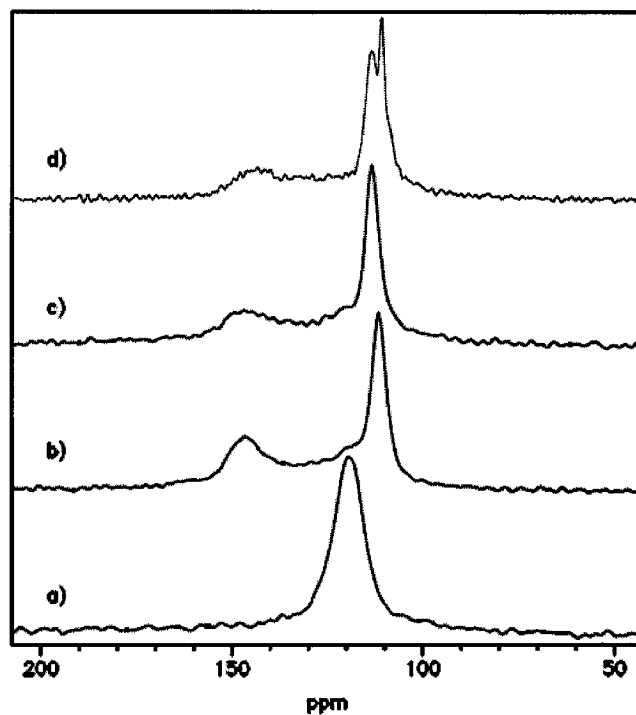
FIGURE 4.3 High resolution ^{13}C MAS NMR spectra at room temperature; (a) magnetically purified empty SWNTs at Larmor frequency (LF) of 50.3 MHz, (b) peapods, sample A at LF of 50.3 MHz, (c) peapods, sample B at LF of 50.3 MHz, and (d) peapods, sample A at LF of 100 MHz.

64

A ^{13}C MAS NMR spectrum on sample A is shown in figure 4.3.(b). Sample A is a peapod sample with 25% ^{13}C enriched C_{60} filled inside the magnetically purified SWNTs. Based on TEM and XRD measurements (see Figure 3.3), a minimum of 70% C_{60} filling ratio will produce a maximum of 16% of the nanotubes contributing to the NMR signal, which corresponds to the broad band at 118.8 ppm. The detailed spectral fitting is presented in figure 4.4. The sharp peak at 111.28 ppm is assigned safely to the encapsulated fullerenes. The narrow peak width (5 ppm) rules out the possibility of SWNTs as the origin, as they have the theoretical FWHM of 20 ppm. Surprisingly, the peak has diamagnetically shifted as much as 36.9 ppm compared to that of bulk fullerenes, due to ring currents on SWNTs. Finally, the peak at 148.18 ppm is assigned to paramagnetically shifted fullerenes by 2 ppm, as defects on the walls of SWNTs generate the paramagnetic ring current [27].

Figure 4.3(c) presents ^{13}C MAS NMR spectrum on sample B, with 16% ^{13}C enriched C_{60} filled inside chemically-purified SWNTs. Despite different purification method by a different group, the spectrum is nearly identical to the one from sample A. The peaks at 112.15 ppm and 147.15 ppm are assigned to diamagnetically and paramagnetically shifted fullerenes, respectively.

Figure 4.3.(d) shows the ^{13}C-MAS NMR spectrum on sample A measured with a Larmor frequency (LF) of 100 MHz. Note that the earlier spectrum (figure 4.3.(b)) was measured with LF of 50.3 MHz. The higher LF frequency resulted in 3 ppm of splitting in the peak at 111 ppm which may be a signature of two different electronic properties of

65

encapsulating SWNTs. The peak at 145 ppm is assigned to the paramagnetically shifted fullerenes.

A spectral fitting for MAS NMR spectrum in figure 4.3(b) is shown in figure 4.4. We developed a program to consider the distribution of paramagnetic shifts from various types of defects on SWNTs as shown in figure 4.4(a). Some fullerenes surrounded by an intact SWNT wall have the full diamagnetic shift of 36.9 ppm, whereas others close to defects on the wall have no diamagnetic shift, but 2 ppm of paramagnetic shift. The nanotubes content was fixed as 16% as shown in figure 4.4(b). The fit was then performed by changing population at each shift. The best fit for the experimental spectrum (figure. 4.4(e)) is shown in figure 4.4(d). The ratio between diamagnetically and paramagnetically shifted fullerenes was calculated to be 2.1: 1 as shown in figure 4.4(c).
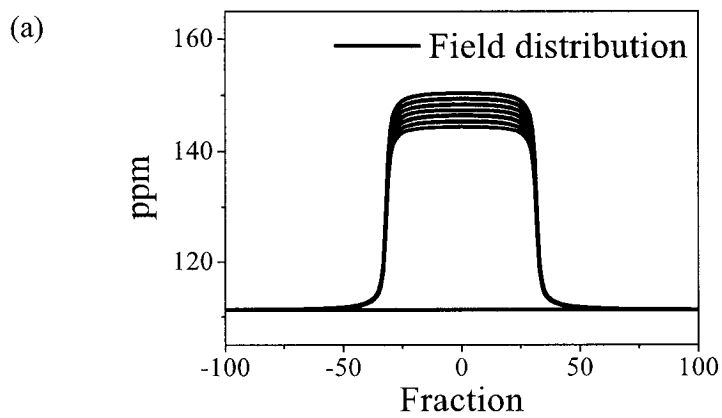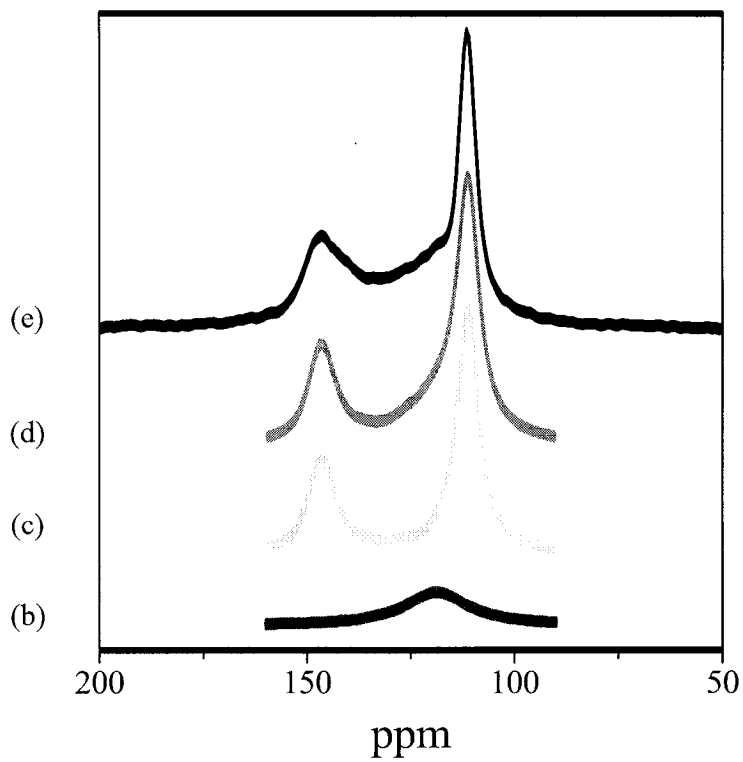
FIGURE 4.4 A fitting of High resolution ^{13}C MAS NMR spectrum of sample A. (a) distribution of diamagnetic shifts due to various types of defects, (b) SWNT content, (c) paramagnetically and diamagnetically shifted fullerenes, (d) fitted curve, and (e) experimental NMR spectrum.

4.4.1.2 DYNAMICS OF ENCAPSULATED FULLERENES

The MAS NMR spectrum for sample A recorded at 4.8 kHz is shown in figure 4.5.(a). The sidebands indicated by stars result from the frozen state of the paramagnetically shifted fullerenes which correspond to the isotropic line at 148.18 ppm. To the contrary, the absence of sidebands corresponding to the isotropic peak at 111.28 ppm indicates the rotation of the diamagnetically shifted fullerenes.

Figure 4.5.(b) shows the static NMR spectrum of sample A. The paramagnetically shifted fullerenes produce chemical shift anisotropy (CSA), shown in the bottom part of the spectrum, to confirm their frozen state. On the top part, a relatively narrow peak is produced by the freely rotating diamagnetically shifted fullerenes. The peak width of around 30 ppm which is still broad compared to the bulk fullerenes (~ 3 ppm) results not from a restricted dynamics of fullerenes, but from anisotropic ring currents on the SWNTs [17,28]. Diamagnetic shielding by a (16,0) nanotube is larger by 7 ppm when the tube axis is perpendicular to the applied magnetic field rather than being parallel. Also, the various types of SWNTs and the larger diameter SWNTs in the current study could broaden the peak further.
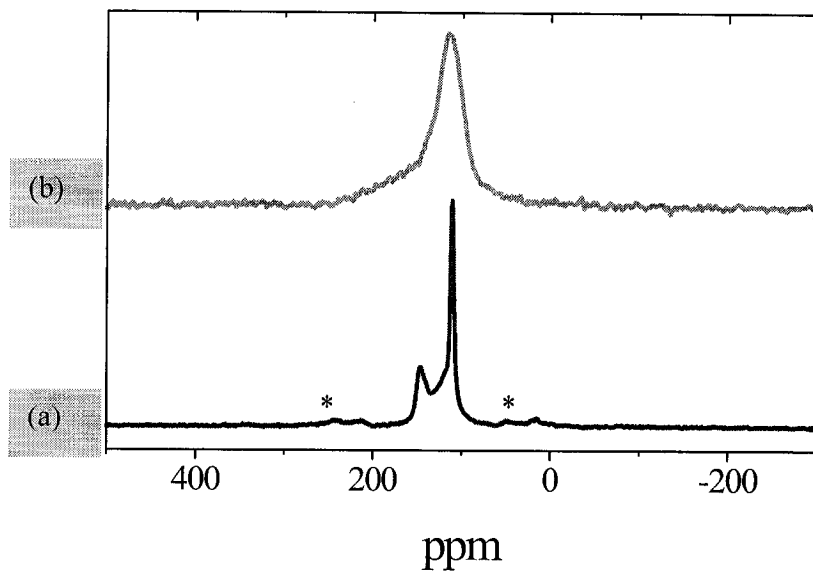
FIGURE 4.5 (a) High resolution ^{13}C MAS NMR spectrum of sample A spun at 4.8 KHz. Stars indicate the side bands of the isotropic shift of paramagnetically shifted fullerenes at 148.18 ppm. (b) Static NMR spectrum of sample A at room temperature.

4.4.1.3 ORIGIN OF THE MAGNETIC SHIFTS IN NMR

Marques *et al.* predicted that a diamagnetic shift of inner nanotubes in the DWNTs is generated by ring currents from π electrons on outer nanotubes [17]. *Ab-initio* calculation and a simple classical model produced the diamagnetic shifts of 21 ppm and 29 ppm, respectively. The 36.9 ppm of the diamagnetic shift in the current study is close to their prediction. The difference may result from the stronger ring currents in our experiment due to the larger diameter SWNTs.

The 3 ppm of splitting in the diamagnetic shift in figure 4.3(d) may result from two different chirality families in semiconducting tubes as predicted by Marques *et al.* [17]. The effect of metallic tubes on the splitting can not be excluded either [17]. More detailed study will be necessary to confirm this.

The paramagnetic shift of 2 ppm can be induced by paramagnetic ring currents generated from localized electrons in defects on SWNT walls [27]. One might speculate that the peak at 148.18 ppm originates from excessive fullerenes stuck outside the nanotubes as 3-D FCC fullerenes have the isotropic line at 143 ppm with FWHM of ~ 3 ppm. However, the possibility is ruled out from the facts that (i) the sample was annealed after the filling step in a dynamic vacuum at 650 °C, (ii) the constant position of the (1,1) XRD peak after fullerene filling confirms no introduction of fullerenes into the interstitial sites in a SWNT bundle, (iii) TEM images show well-filled SWNT bundles with clean surface, and (iv) there is absolutely no NMR signature of excessive FCC C_{60} bulk.

4.4.1.4 THE CRITICAL ROLE OF DEFECTS IN SWNTs

Our NMR studies suggest that defects not only destroy the magnetic shielding of fullerenes by SWNTs, but they also freeze fullerenes. They could provide a preferential position for fullerenes to rest by breaking the perfect symmetry of Van der Waals interaction with a SWNT wall. Localized electrons on defects might have catalyzed the dimerization or polymerization of fullerenes during the peapod preparation. Raman and neutron scattering studies indeed showed that as-prepared peapods were made of monomer, dimer, and polymer [29,30]. In the current NMR study, however, no sp^3 line between 50 ppm and 70 ppm was observed. The small fraction, one or two out of sixty, as well as the long relaxation time of sp^3 carbon would make their detection nearly impossible, even if some of fullerenes in our peapods had been polymerized.

4.4.2 DYNAMICS OF C_{60} ENCAPSULATED IN SWNTs

4.4.2.1 THE SPIN-LATTICE RELAXATION STUDY

The saturation-recovery magnetization curve of peapod sample A at room temperature is shown Figure 4.6. The double exponential decay fitting using the equation-(4.1) resulted in the relaxation times of 43 sec and 3 sec with the contents of 81% and 19%, respectively. The long component relaxation time originates from encapsulated fullerenes whose content is also calculated to be a minimum of 84%, in the sample with 25% ^{13}C enriched fullerenes filled into natural carbon based SWNTs with minimum efficiency of 70% (figure 3.3.(c)). The dynamics of 1-D fullerenes encapsulated in SWNTs can be studied by analyzing the long component T_1.
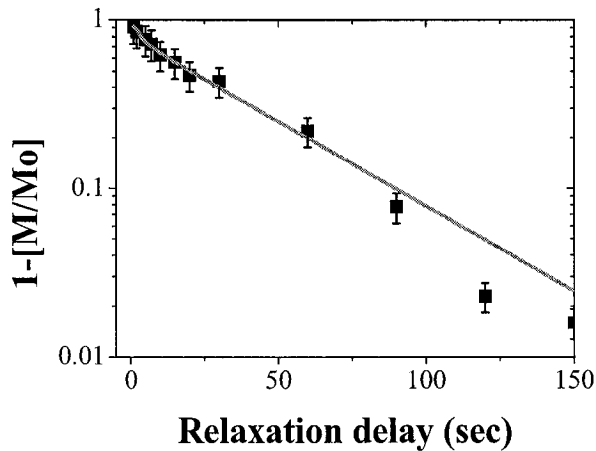
FIGURE 4.6 Magnetization recovery of peapods as a function of relaxation delay at room temperature. Fit corresponds to double exponential decay in spin-lattice relaxation of peapods.

72

The long component, T_1 in spin lattice relaxation measurements in peapods is shown in figure 4.7. The general trend is similar to that in 3-D bulk fullerenes [5]. In 3-D, the fullerene molecules perform free rotation from room temperature to 260 K. Below 260 K, the free rotation changes to hindered rotation due to orientational ordering, resulting in sudden decrease in T_1 [4]. Further, the fullerene molecules stop rotating below ~ 100 K. To the contrary, the sudden drop of T_1 in 1-D fullerenes surprisingly occurs at ~ 100 K which is lower than in 3-D solid by as much as ~ 160 K. Following those previous studies on the phase transition [4,5], we suggest that 1-D fullerenes change their dynamics from free rotation to hindered rotation at ~ 100 K, which can be fitted by two separate variable sets as will be discussed in section 4.4.2.4.
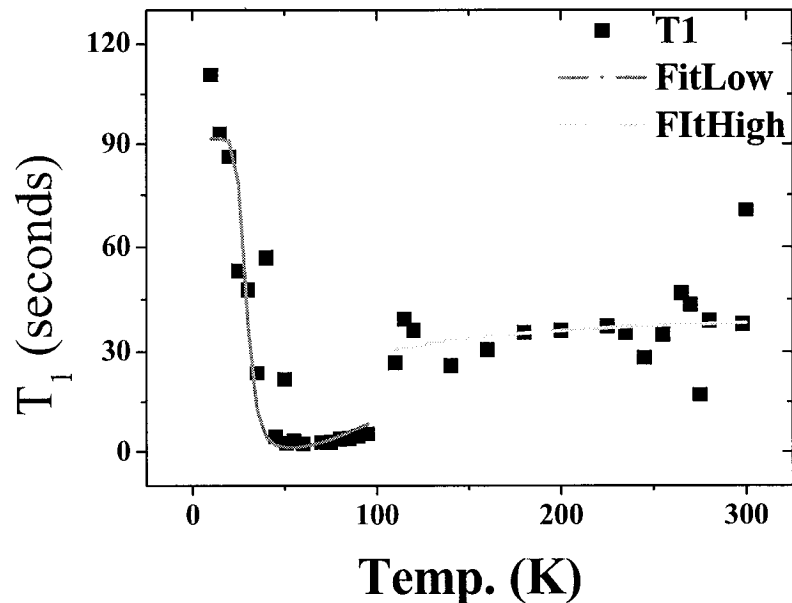
FIGURE 4.7 Spin-lattice relaxation time of peapods as a function of temperature. The dynamics of encapsulated 1-D fullerenes in peapods changes from free to hindered rotation at 100 K.

4.4.2.2. STATIC NMR MEASUREMENTS ON PEAPODs

The static NMR spectra of peapods in the temperature range of 5 K – 300 K are shown in figure 4.8(a). The spectrum at room temperature can be deconvoluted into the sharp feature at 111.28 ppm and into the typical powder pattern underneath it. The former is assigned to diamagnetically shifted-freely-rotating fullerenes as the peak broadens below 40 K, due to the change in their dynamics. To the contrary, little change in the latter with temperature indicates a frozen state of paramagnetically shifted fullerenes at room temperature.

Now, let us focus on the narrow line at 111.28 ppm. It changes little down to 40 K despite the dynamics transition from free rotation to hindered rotation at 100 K. The hindered rotation should be fast enough to average the chemical shift anisotropy (CSA) out. Below 30 K, the shoulder at ~180 ppm grows at the expense of the peak at 111.28 ppm, as some fullerenes start to freeze. At ~15 K, a typical static powder pattern is developed and all the fullerene molecules have been frozen. Astonishingly, the freezing temperature of 1-D fullerenes, ~ 30 K is much lower than that observed for 3-D solid, which has been shown to be in the range of 150 K-90 K [6,7].
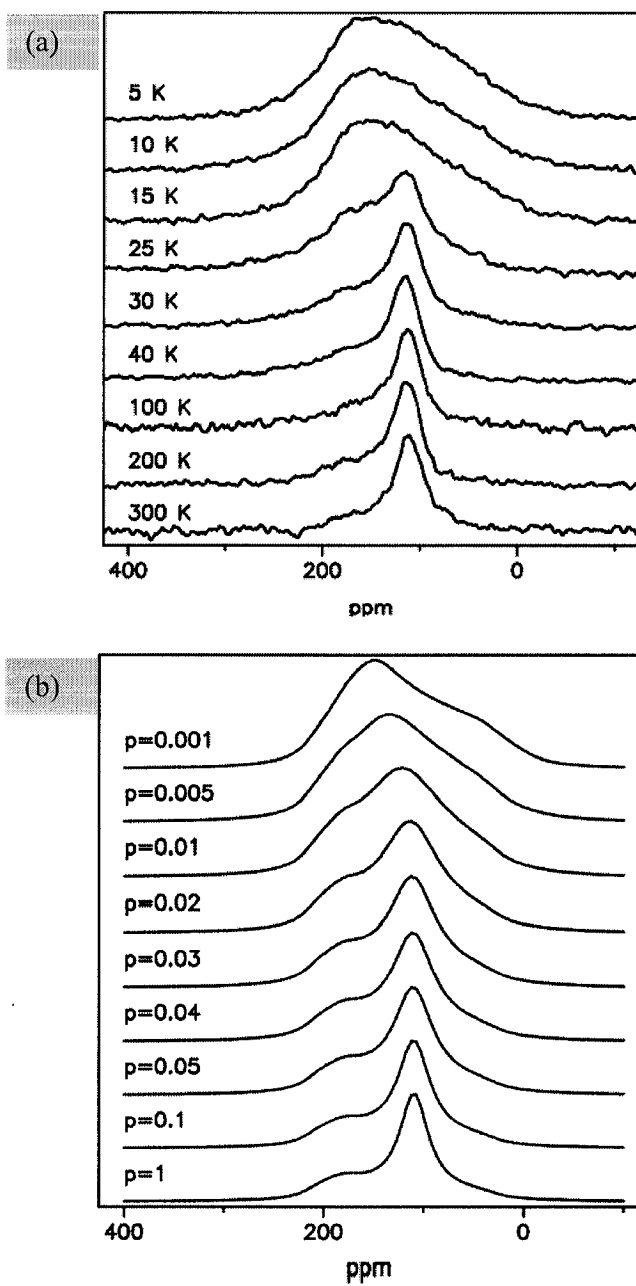
FIGURE 4.8 Static NMR spectra and simulation of peapods as a function of temperature. (a) the sharp peak at 111.28 ppm corresponding to rotating fullerenes broadens below 30 K as they start to freeze. (b) Simulation using random jump model. The variable, p, is a probability for a jump of a nuclear spin and inversely proportional to the correlation time, τ.

The experimental static NMR spectra have been simulated successfully. Figure 4.9 shows the simulation for the static spectrum at room temperature. Based on the assignments above, the curve (a) represents paramagnetically shifted fullerenes which have been frozen at room temperature. In order to simulate freely-rotating diamagnetically shifted fullerenes, the curve (a) is shifted diamagnetically by 36.9 ppm as shown in the curve (b). The rotation of a fullerene is incorporated by the random jump model where a nuclear spin can jump to any site on the fullerene with a probability of p. A probability is proportional to the speed of fullerene rotation and also to the inverse of correlation time, τ. As a result, the freely-rotating fullerenes with the diamagnetic shift of 36.9 ppm could be simulated as shown in the curve (c). The complete fit is then obtained by the sum of the curves (a) and (c) with the fraction of 4 to 6, respectively, as shown in the curve (d). The final fitting matches well the experimental spectrum (e). Over all temperature range, the static NMR spectra have been simulated successfully by changing the probability as shown in figure 4.8(b).
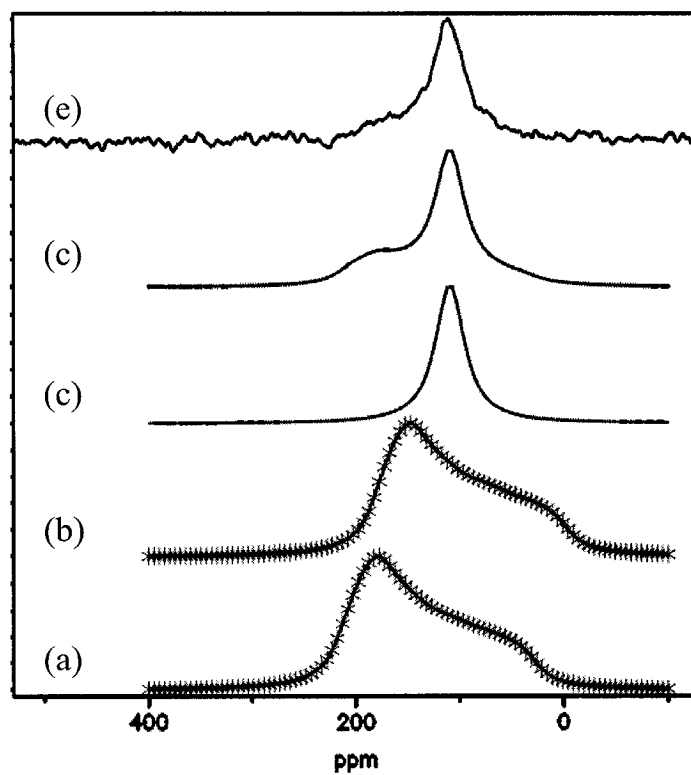
Figure 4.9 A fitting of the static NMR spectrum at room temperature. (a) A CSA of a frozen C_{60} with the paramagnetic shift of 2 ppm. (b) A CSA of a frozen C_{60} with the diamagnetic shift of 36.9 ppm. (c) The isotropic peak after applying the random-jump model with the probability of 1 to the curve (b). (d) The sum of the curves (a) and (c) with the fraction of 4:6. (e) The experimental spectrum.

4.4.2.3 SPIN-SPIN RELAXATION AND THE SECOND MOMENT

The behavior of spin-spin relaxation (T_2) and the second moment ($\delta\omega$) are shown in figure 4.10 and its inset respectively. As the measurements are sensitive to the difference among the Larmor frequencies of nuclear spins in a sample, the freezing of 1-D fullerenes in terms of NMR acquisition time occurs explicitly at 30 K where both T_2 rate and $\delta\omega$ start to increase.
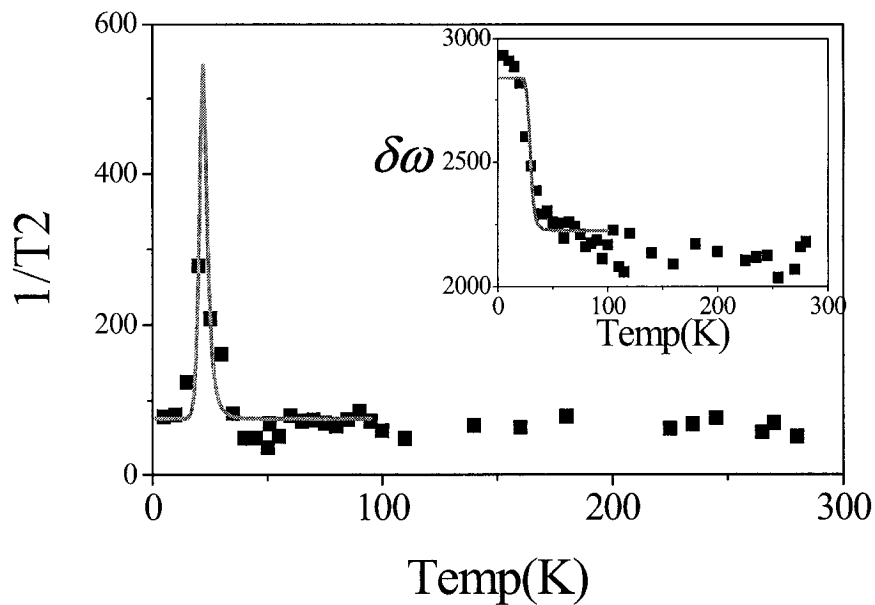
FIGURE 4.10 the spin-spin relaxation time of peapods and the second moment in the inset. Encapsulated fullerenes start to freeze at 30 K.

The fluctuating magnetic field induced from the chemical shift anisotropy of rotating fullerenes dominates spin-lattice relaxation behavior in peapods. The relaxation time, T_1 could be fitted with the equation-(4.2) [5,31,32],

$$\frac{1}{T_1} = \frac{6}{40} \times \Delta\omega^2 \times \frac{2\tau}{\left(1 + \omega_0^2 \tau^2\right)} \tag{4.2}$$

where $\Delta\omega$ is the change of CSA at phase transition and τ is correlation time, which is following Arrhenius behavior, given by

$$\tau = \tau_0 \exp\left(\frac{\Delta E}{k_B T}\right) \tag{4.3}$$

where τ_0 is autocorrelation time at a infinite temperature, ΔE is activation energy, and ω_0 is Larmor frequency for ^{13}C.

Separate sets of variables were used to fit the data over the whole temperature region. Below 100 K, the fitting (the red curve in figure 4.7) produced the activation energy of 27 meV for the hindered rotation. From 300 K to 100 K, the fitting (the green curve in figure 4.7) produced the activation energy of 8 meV for the free rotation.

As shown in figure 4.10, T_2 rate could be fitted using the equation given by [31],

$$\frac{1}{T_2} = \frac{1}{40} \times \Delta\omega^2 \times \left(3J(\omega_0) + 4J(0)\right) \tag{4.4}$$

where, the spectral density $J(\omega_o)$ and $J(0)$ are given by

$$J(\omega_0) = \frac{2\tau}{\left(1 + \omega_0^2 \tau^2\right)}$$

$$J(0) = \frac{2\tau}{\left(1 + \Delta\omega^2 \tau^2\right)} \qquad (4.5)$$

The fitting in the temperature range from 5 K to 95 K produced the activation energy of 28 meV for the hindered rotation. The nearly same magnitude as that obtained from T_1 measurement indicates there is no further change in dynamics below ~ 100 K.

The second moment, $\delta\omega$, was fitted in the temperature range from 5 K to 95 K using the following expression [31],

$$\left(\delta\omega\right)^2 = \left(\delta\omega''\right)^2 + \left(\delta\omega'\right)^2 \times 2\pi \times \arctan\left(\alpha\tau(\delta\omega)\right) \qquad (4.6)$$

where, α is equal to one, and $\delta\omega''$ and $\delta\omega'$ are the linewidths at high temperature and low temperature, respectively. The fitting produced the activation energy of 35 meV for hindered rotation.

Table 1 summarizes the fitting results for T_1, T_2, and $\delta\omega$ in the 1-D encapsulated fullerenes along with T_1 in the 3-D bulk solid for comparison. The activation energies for the hindered rotation in 1-D fullerenes obtained from T_1, T_2, and $\delta\omega$ are 27 meV, 28 meV, and 35 meV respectively. The narrow distribution of the activation energies in the different measurements compensates any inaccuracy in the values due to error range with the fittings. The average value, 30 meV is almost one eighth of that in 3-D solid, (250 meV). Also, the activation energy for the free rotation in 1-D encapsulated fullerenes, 8 meV is one fifth of that in 3-D solid (42 meV). Yildirim *et al.* has predicted that in 3-D solid, a single or double bond in a fullerene prefers to face a center of a pentagon or a hexagon in a neighboring fullerene to maximize Coulomb attraction [8]. Therefore, the

activation energy for a rotation, which is a function of Van der Waals interaction as well as the Coulomb attraction, would be proportional to the number of nearest neighbors. The ratio of the number of nearest neighbors in 1-D to that in 3-D of one sixth is consistent with the ratios of activation energies between 1-D and 3-D systems obtained above, which turn our to be one fifth and one eighth.

TABLE 4.1 Activation energy ΔE, autocorrelation time τ_0, change of CSA at phase transition $\Delta\omega$, and corresponding T_1, T_2, and $\delta\omega$ in 1-D and FCC fullerenes.

	T_1 in 1-D fullerenes		T_2 in 1-D fullerenes	$\delta\omega$ in 1-D fullerenes	T_1 in 3-D Bulk [5]	
Fitting range (K)	5-100	100-300	5-100	5-100	193-243	263-323
$\Delta\omega$	15968	21774	4694	17891	-	-
ΔE (meV)	27	8	28	35	250	42
τ_0 (sec)	5×10^{-11}	5×10^{-11}	5×10^{-11}	5×10^{-11}	3×10^{-14}	5×10^{-12}

The interaction between fullerenes and SWNTs should not be neglected. Van der Waals interaction, potential Coulomb interaction, and a small charge transfer between them may have resulted in a drop in T_1, which otherwise would be smooth in a 1-D system. [33,34]. It is also possible that frozen fullerenes at room temperature, whose fraction is as much as 30%, may have provided a fairly uniform environment to result in the first order transition-type dynamics change.

4.4.3 CONCLUSIONS

Using the novel magnetically purified SWNTs and 25% ^{13}C enriched fullerenes, the local magnetic property of SWNTs and the dynamics of 1-D fullerenes were investigated using NMR spectroscopy. Surprisingly, encapsulated fullerenes experience 36.9 ppm of magnetic shielding due to the ring currents by the π electrons on SWNTs. The diamagnetic shielding could be destroyed by the paramagnetic currents from defects on the walls of SWNTs. The encapsulated fullerenes showed the unique 1-D dynamics where the dynamics transition temperature reduces from ~ 260 K in 3-D solid to ~ 100 K in 1-D case. The significant decrease in the dynamics transition temperature results from the reduction of the nearest neighbors from twelve to two, which is consistent with the ratios of activation energies for rotations in 1-D fullerenes to those in 3-D solid.

4.5.1 WELL DEVELOPED DWNTs PRODUCED FROM PEAPODs

Raman measurements are carried out on high temperature annealed peapod samples, which are known to turn into DWNTs. Figure 4. 11 shows the Raman spectra of SWNTs, peapods, and DWNTs. Magnetically purified SWNTs which were annealed at 1250 °C for 24 hours produced typical RBM bands at 147 cm^{-1} and 163 cm^{-1} (see the green spectrum).
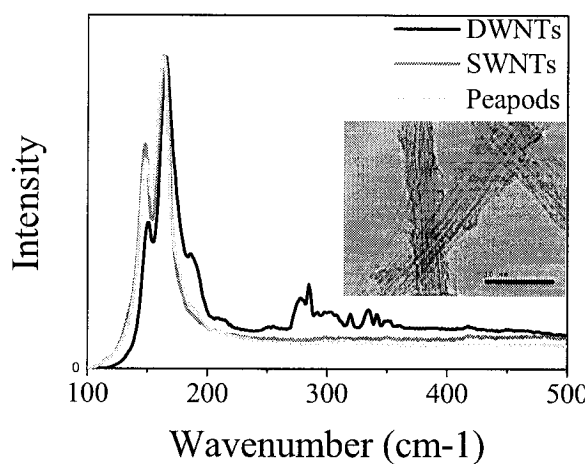
FIGURE 4.10 Raman spectra using 633 nm laser of magnetically purified SWNTs (the red curve), peapods (the green curve) and DWNTs, obtained by annealing peapods at 1250°C for 24 hours, (the black curve). Inset shows the TEM image of DWNTs formed after the annealing step.

The Raman spectrum of peapods in red curve is nearly identical to that of SWNTs. DWNTs which were produced through a high temperature annealing of peapods at 1250 °C for 48 hours show additional Raman features in the spectral region of 250-350 cm^{-1} (shown in the black spectrum). They originate from fullerene-induced inner nanotubes whose average diameter is calculated to be 0.75 nm (0.84 nm - 0.66 nm), using the equation 2.3. The inset shows a typical TEM image of well-developed DWNTs where the average diameter of inner tubes is measured as 0.78 nm.

4.5.2 ^{13}C MAS NMR SPECTRA

We have carried out ^{13}C MAS NMR experiments using Hahn echo synchronized with a rotor spinning at 10 kHz on peapods and DWNTs, and the results are shown in Figure 4.12 (a) and (b) respectively. With the realization of ferromagnetic catalyst free SWNTs and the high filling ratio of 25% ^{13}C enriched fullerenes, the well-resolved spectrum on peapods could be observed for the first time, as described in chapter 4.4. Briefly speaking, there are three distinctive components for SWNTs, diamagnetically shifted, and paramagnetically shifted fullerenes. The peak at 118.8 ppm is assigned to SWNTs, consistent with theoretical and experimental studies [23-26]. The sharp peak at 111.28 ppm is assigned to freely rotating fullerenes inside SWNTs. Surprisingly, the encapsulated fullerenes have been diamagnetically shifted by 36.9 ppm compared to those in bulk phase due to magnetic shielding caused by the ring currents on SWNTs. The third component at 148.18 ppm is assigned to encapsulated fullerenes close to the

defects. Paramagnetic currents generated by local electrons at defects cancel diamagnetic

ring currents [27].
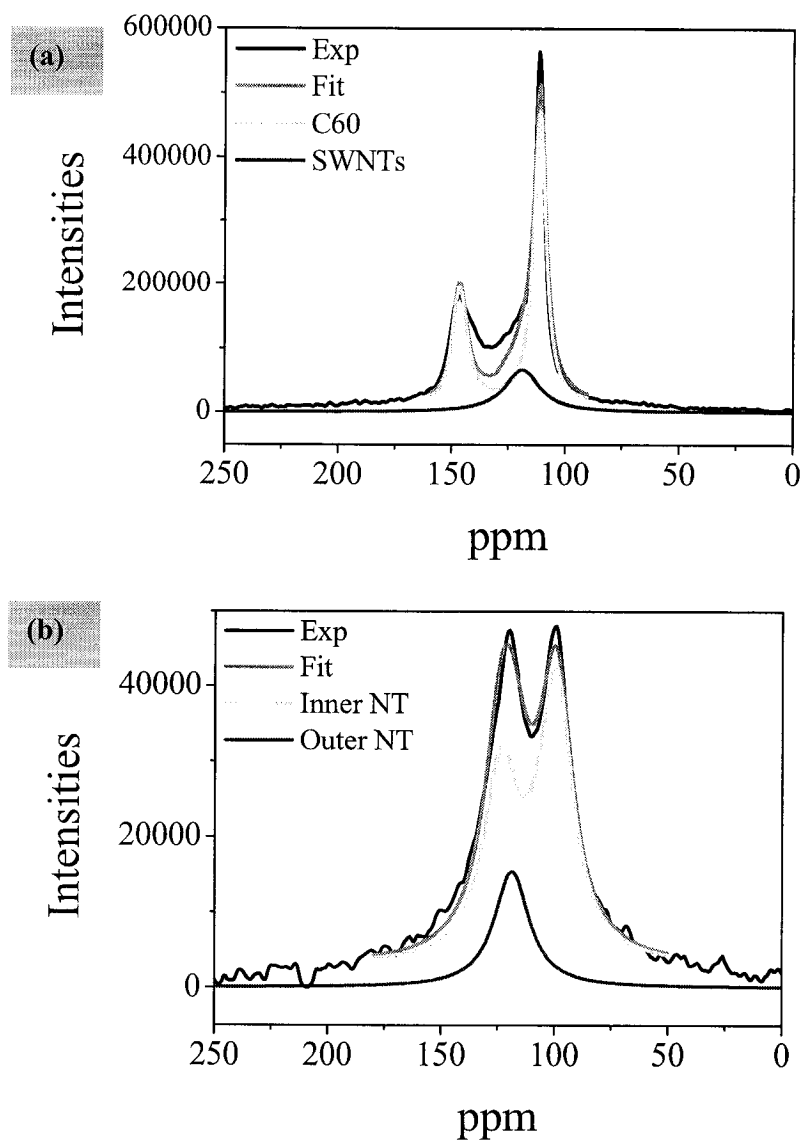
FIGURE 4.12 High resolution ^{13}C MAS NMR spectra of (a) peapods and (b) DWNTs.

Figure 4.12 (b) shows ^{13}C MAS NMR spectrum on DWNTs. The earlier NMR measurement on DWNTs performed by Singer *et al.* produced a single broad peak at 120 ppm with FWHM of 100 ppm, contrary to the prediction of two NMR peaks, one at ~100 ppm and the other at ~ 120 ppm [17,18]. We report here, for the first time, two well-resolved NMR peaks on DWNTs. Since fullerenes will not escape SWNTs during the annealing process of peapods, the signal intensities of inner and outer nanotubes in DWNTs will be the same as those of encapsulated fullerenes and SWNTs in peapods. With the content and peak position of outer nanotubes fixed as 16% and 118.8 ppm, the spectrum was fitted successfully with three components, paramagnetically shifted inner nanotubes at 125.8 ppm, outer nanotubes at 118.8 ppm, and diamagnetically shifted inner nanotubes at 99.18 ppm, as shown in figure 4. 11(b).

The 26.62 ppm of diamagnetic shift of inner nanotube is generated by diamagnetic ring currents from π electrons on outer nanotubes, similar to as in the case of peapods. However, the shift 26.62 ppm in DWNTs is smaller than that in peapods. In the current study, the magnitude of a diamagnetic shift is measured by the gap between a non-shifted (or paramagnetically shifted) peak and a diamagnetically shifted peak. The former shift is sensitive to the content of defects on outer nanotubes. The lesser number of defects on the outer nanotubes in DWNTs than those in peapods will lead to the smaller paramagnetic shift, and hence the smaller gap. This is due to the heat treatment during the DWNT production.

The smaller diamagnetic shift in DWNTs than that in peapods may also result from the different coupling of ring currents in outer nanotubes with those in encapsulated

materials. Inner nanotubes in DWNTs are composed of hexagons only to produce diamagnetic ring currents, whereas fullerenes in peapods have pentagons along with hexagons to produce paramagnetic as well as diamagnetic ring currents. The complicated interaction between the different types of ring currents needs careful theoretical studies.

The paramagnetic shift of ~ 5 ppm in the inner nanotubes (125.8 ppm), relative to the outer nanotubes (118.8 ppm), is expected due to the smaller curvature in the former which will modify the electronic structure of π orbital [35].

Spin lattice relaxation time measurements on DWNTs have been carried out at room temperature. As shown in figure 4.13, a double exponential decay fitting using equation (4.1) yields two relaxation times, 0.2 sec and 5 sec, with fractional contribution of 25% and 75%, respectively. Since the fractions did not fluctuate significantly with temperature, we fitted relaxation data using the fixed ratio of 25% : 75% over all the temperature range to remove unnecessary error. In this study, we focus on the long component, the main part of the relaxation.
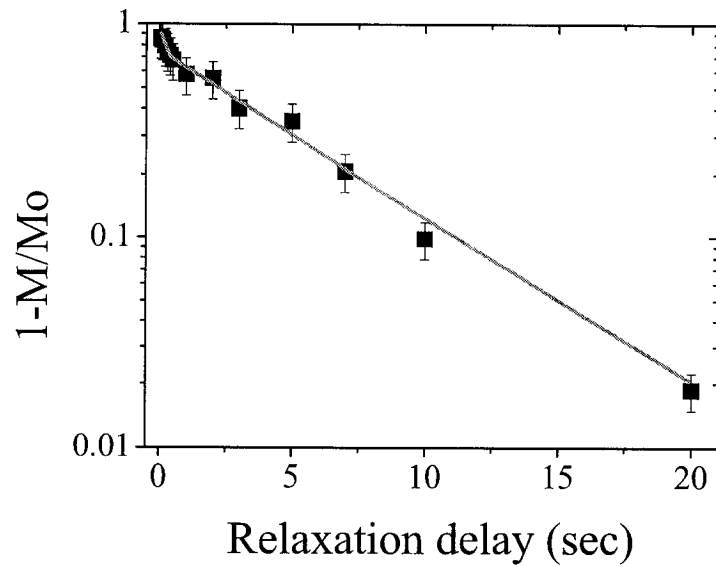
FIGURE 4.13 Spin-lattice relaxation of DWNTs at room temperature. Fit corresponds to double exponential decay in the spin-lattice relaxation.

In figure 4. 14(a) we show the plot of $\dfrac{1}{T_{1long}T}$ as a function of temperature, where

T_{1long} is the long component in the relaxation rate. The constant value of $\dfrac{1}{T_{1long}T}$ down to

~ 20 K is a typical metallic behavior. The sudden increase below ~ 20K could be a

signature of spin gap in metallic inner nanotubes as reported by Singer *et al.* [18].

The plot of $\dfrac{1}{T_{1short}T}$ is shown in figure 4. 14 (b), where T_{1short} is the short

component, only 25% of the relaxation rate. The increase of $\dfrac{1}{T_{1short}T}$ at low temperature

and the subsequent saturation may be related to defects on outer nanotubes. More

experiments are under progress.
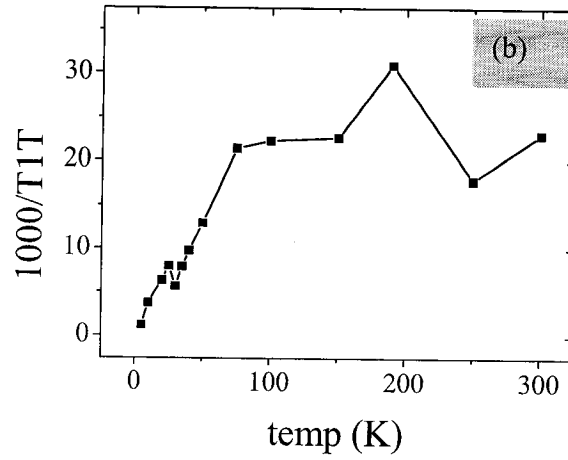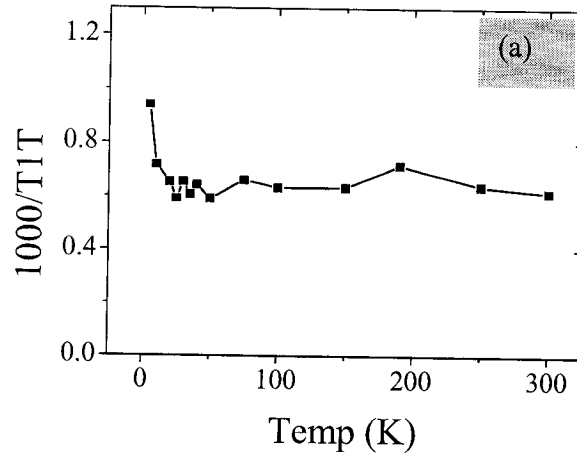
FIGURE 4.14 Spin-lattice relaxation time T_1 of DWNTs as a function of temperature. $\dfrac{1}{T_1 T}$ vs. temperature graph for (a) long component and (b) short component in double exponential decay fitting.

From the Korringa behavior in figure 4. 14 (a), DOS at Fermi level of metallic inner nanotubes can be obtained using the following equation and compared with a theoretical value to verify the origin of this long relaxation component.

$$\left\langle \frac{1}{T_1 T} \right\rangle = \frac{2\pi k_B}{\hbar} \times A_{iso}^2 \times DOS(E_f)^2 \text{ and } A_{iso} = \frac{2}{5} \times \gamma_e \gamma_n \frac{\hbar^2}{r^3} \qquad (4.7)$$

where, A_{iso} is the isotropic hyperfine coupling constant, and γ_e and γ_n are the gyromagnetic ratios of the electron and nuclear spin, respectively [23,32,36]. By using 8.2×10^{-7} eV for A_{iso}, DOS(E_f) is calculated to be 0.033 states/(eV×spin×atom) [23,32]. The theoretical DOS(E_f) for (6,6) armchair nanotubes, whose chirality corresponds to average inner nanotubes in our samples is 0.025 states/(eV×spin×atom) [35,37]. The small difference may result from the interaction between inner and outer tubes, which will be discussed in the following paragraph.

The increase of $\dfrac{1}{T_{1long}T}$ below 20 K in figure 4.14(a) might be a signature of spin-gap as observed by Singer $et\ al.$ [18]. Our earlier electron spin resonance (ESR) studies on DWNTs show that electron susceptibility increases below 20 K before decreasing further at 7 K, possibly due to the spin gap [38]. The slight increase of $\dfrac{1}{T_{1long}T}$ below 20 K could be the starting point of the spin-gap.

In a random distribution, one third of SWNTs should be metallic and the other two thirds should be semiconductors. High fraction of metallic inner nanotubes (75%) in the current study as well as in the reference 18 is not understood easily. Okada $et\ al.$ predicted that a (7,0) semiconducting nanotube encapsulated by another semiconducting

91

nanotube may become metallic, due to curvature-induced rehybridization between π and σ states [39,40]. When both inner and outer nanotubes are metallic, outer nanotubes are predicted to donate electrons to the inner nanotubes [41]. HRTEM studies on DWNTs performed by Hashimoto *et al.* confirmed a strong interaction between the inner and outer nanotubes, and this has been the reason for corrugation of graphene layers in nanotubes [42]. All such interactions between inner and outer nanotubes in DWNTs will favor the former to have metallic characteristic, which could lead to the high fraction of the metallic nanotubes, as observed in the current studies. The same reasoning could be applied for the understanding of the difference between DOS of (6,6) nanotubes obtained from the current studies and theoretical studies.

The origin for the behavior of the 25% short relaxation component needs further more experiments. However, we can exclude a few potential sources for this behavior. The small content of impurities in the sample, such as amorphous carbon or graphitic onion particles, cannot produce 25% of the NMR signal. In chapter 3, nanotube content in magnetically purified SWNTs was measured to be 50-70% [22]. The minimum of 70% filling efficiency of 25% ^{13}C enriched fullerene in peapods results in only a maximum 14% of impurity contribution to an NMR signal. Moreover, 50% of the relaxation signal in the magnetically purified nanotubes would have shown such a fast relaxation if impurities were the origin of the short component.

Metallic inner nanotubes are not responsible for the short component either. Following the Korringa law in the equation-(4.7), the value of $1/T_1T$ is proportional to the square of $DOS(E_f)$. Since it is inversely proportional to the diameter of nanotubes [35,37],

a 0.8 nm metallic inner nanotube would have 2 times higher DOS than a 1.4 nm metallic outer nanotube, producing the maximum of 4 times faster relaxation time in the inner nanotube. In the current study, 15 times faster relaxation time in inner nanotubes than in outer nanotubes is well beyond this range.

4.5.4 CONCLUSIONS

^{13}C MAS NMR on DWNTs produced two well resolved isotropic shifts. The one at 99.18 ppm corresponds to diamagnetically shifted inner nanotubes, due to ring currents on outer nanotubes. The other isotropic shift at ~ 120 ppm could be deconvoluted into two contributions from paramagnetically shifted inner nanotubes at 125.8 ppm and from the outer nanotubes at 118.8 ppm. Spin-lattice relaxation studies revealed high fraction (75%) of the inner nanotubes to be metallic, possibly due to the strong interaction with the outer nanotubes.

93

1. H. W. Kroto, J. R. Heath, S. C. O'Brien, R. F. Curl, and R. E. Smalley, Nature, **318**, 162 (1985).

2. L.J. Dunne, A.K. Sarkar, H.W. Kroto, J. Munn, P. Kathirgamanathan, U. Heinen, J. Fernandez, J. Hare, D.G. Reid, and A.D. Clark, J. Phys.: Condens. Matter **8**, 2127 (1996).

3. S.R. Wilson, in: K. Kadish, R. Ruoff (Eds.), *The Fullerene Handbook*, Wiley, New York, (2000).

4. P. A. Heiney, J. E. Fischer, A. R. McGhie, W. J. Romanow, A. M. Denenstein, J. P. McCauley, Jr., and A. B. Smith, Phys. Rev. Lett. **66**, 2911 (1991).

5. R. Tycko, G. Dabbagh, R. M. Fleming, R. C. Haddon, A. V. Makhija, and S. M. Zahurak, Phys. Rev. Lett. **67**, 1886 (1991).

6. R. Blinc, J. Seliger, J. Dolinsek, and D. Arcon, Phys. Rev. B **49**, 4993 (1994).

7. R. Tycko, R. C. Haddon, G. Dabbagh, S. H. Glarum, D. C. Douglass, and A. M. Mujsce, J. Phys. Chem. **95**, 518 (1991).

8. T. Yildirim, A. B. Harris, and S. C. Erwin, Phys. Rev. B **48**, 1888 (1993).

9. E. D. Minot, Y. Yaish, V. Sazonova, and P. L. McEuen, Nature **428**, 536 (2004).

10. M. E. Itkis, S. Niyogi, M. E. Meng, M. A. Hamon, H. Hu, and R. C. Haddon, Nano Lett. **2**, 155 (2002).

11. R. Saito, M. Fujita, G. Dresselhaus, and M. S. Dresselhaus, Appl. Phys. Lett. **60**, 2204 (1992).

12. H. Ishii, H. Kataura, H. Shiozawa, H. Yoshioka, H. Otsubo, Y. Takayama, T. Miyahara, S. Suzuki, Y. Achiba, M. Nakatake, T. Narimura, M. Higashiguchi, K. Shimada, H. Namatame, and M. Taniguchi, *Nature* **426**, 540 (2003).

13. A. Javey, J. Guo, Q. Wang, M. Lundstrom, and H. Dai, Nature **424**, 654 (2003)

14. D. J. Hornbaker, S.-J. Khang, S. Misra, B. W. Smith, A. T. Johnson, E. J. Mele, D. E. Luzzi, and A. Yazdani, Science **295**, 828 (2002).

15. B. W. Smith, M. Monthioux, and D. E. Luzzi, Nature **396**, 323 (1998).

16. M. M. Calbi, M. W. Cole, S. M. Gatica, M. J. Bojan, and G. Stan, Rev. Mod. Phys. 73, 857 (2001).

17. M. A. L. Marques, M. d'Avezac, and F. Mauri, Phys. Rev. B, **73**, 125433 (2006).

18. P. M. Singer, P. Wzietek, H. Alloul, F. Simon, and H. Kuzmany, Phys. Rev. Lett. **95**, 236403 (2005).

19. A. Kleinhammes, S.-H. Mao, X.-J. Yang, X.-P. Tang, H. Shimoda, J. P. Lu, O. Zhou, and Y. Wu, Phys. Rev. B **68**, 075418 (2003).

20. K. Matsuda, T. Hibi, H. Kadowaki, H. Kataura, and Y. Maniwa, Phys. Rev. B **74**, 073415 (2006).

21. Y. Kim, and D. E. Luzzi, J. phys. Chem. B., **109**, 16636 (2005).

22. Y. Kim, O. N. Torrens, J. M. Kikkawa, E. Abou-Hamad, C. Goze-Bac, and D. E. Luzzi, Chem. Mater., **19** (12), 2982 (2007).

23. X. P. Tang, A. Kleinhammes, H. Shimoda, L. Fleming, K. Y. Bennoune, S. Sinha, C. Bower, O. Zhou, and Y. Wu, Science, **288**, 492 (2000).

24. C. Goze-Bac, S. Latil, L. Vaccarini, P. Bernier, P. Gaveau, S. Tahir, V. Micholet, R. Aznar, A. Rubio, K. Metenier, and F. Beguin, Phys. Rev. B, **63**, 100302 (2001).

25. C. Goze-Bac, S. Latil, P. Lauginie, V. Jourdain, J. Conard, L. Duclaux, A. Rubio, and P. Bernier, Carbon, **40**, 1825 (2002).

26. N. A. Besley, J. J. Titman, and M. D. Wright, J. Am. Chem. Soc., **127**, 17948 (2005).

27. F. López-Urías, J.A. Rodríguez-Manzo, E. Muñoz-Sandoval, M. Terrones, and H. Terrones, Optical Materials, **29**, 110 (2006).

28. O. N. Torrens, D. E. Milkie, H. Y. Ban, M. Zheng, G. Bibiana Onoa, T. D. Gierke, and J. M. Kikkawa, J. Am. Chem. Soc., **129** (2), 252 (2007).

29. J. Cambedouzou, S. Rols, R. Almairac, and J.-L. Sauvajol, H. Kataura, and H. Schober, Phys. Rev. B **71**, 041403 (2005).

30. H. Kataura, Y. Maniwa, M. Abe, A. Fujiwara, T. Kodama, K., Kikuchi, H. Imahori, Y. Misaki, S. Suzuki, and Y. Achiba, Appl. Phys. A: Mater. Sci. Process. A **74**, 349 (2002).

31. M. Mehring, *Princiles of high resolution NMR in solids*, Springer-Verlag, Berlin Heidelberg, New York (1983).

32. M. Schmid, C. Goze-Bac, S. Krämer, S. Roth, M. Mehring, C. Mathis, and P. Petit, Phys. Rev. B **74**, 073416 (2006).

33. L. A. Girifalco, M. Hodak, and R. S. Lee, Phys. Rev. B **62**, 13104 (2000).

34. M. Hodak, and L. A. Girifalco, Phys. Rev. B **68**, 085405 (2003).

35. J. W. Mintmire, and C. T. White, Appl. Phys. A **67**, 65(1998).

36. A. Abragam, *Principles of Nuclear Magnetism*, Oxford University Press, Oxford, (1989).

37. R. Saito, R. Matsuo, T. Kimura, G. Dresselhaus, and M. S. Dresselhaus, Chem. Phys. Lett. **348**, 187 (2001).

38. B. Náfrádi, N. M. Nemes, T. Fehér, L. Forró, Y. Kim, J. E. Fischer, D. E. Luzzi, F. Simon, and H. Kuzmany, Phys. Stat. Sol. (b) **243**, 3106 (2006).

39. S. Okada, and A. Oshiyama, Phys. Rev. Lett. **91**, 216801 (2003).

40. W. Song, M. Ni, J. Lu, Z. Gao, S. Nagase, D. Yu, H. Ye, and X. Zhang, Chem. Phys. Lett. **414**, 429 (2005).

41. Y. Miyamoto, S. Saito, and D. Tomanek, Phys. Rev. B. **65**, 041402 (2001).

42. A. Hashimoto, K. Suenaga, Koki Urita, T. Shimada, T. Sugai, S. Bandow, H. Shinohara, and S. Iijima, Phys. Rev. Lett. **94**, 045504 (2005).

CHAPTER 5

SWNTs as NOVEL TUNABLE NANO-MAGNETIC SHIELDER

5.1 INTRODUCTION

Carbon can have various structures due to the hybridization of s and p orbitals. A diamond structure is formed when one s orbital and three p orbitals are hybridized to form sp^3 orbitals, which form four sigma covalent bonds. When one s orbital and two p orbitals are hybridized to form sp^2 orbitals, graphite structure forms, having 3 sigma bonds and leaving the other electron in p orbital delocalized, which forms π bond. These itinerant π electrons produce a ring current under a magnetic field by which graphite has a strong diamagnetic property.

In 1985, Kroto et al. discovered a new unique structure of carbon clusters, C_{60} fullerenes, which are composed of 12 pentagons and 20 hexagons [1]. Contrary to the expectation of huge diamagnetic property for fullerenes due to the ring currents flowing on 20 hexagons, vanishingly small diamagnetism was found [2-6]. Using the London theory, paramagnetic currents flowing in pentagons in C_{60} were found to be strong enough to cancel the diamagnetic currents in hexagons [4,5]. Therefore, diamagnetism is expected to be proportional to the ratio of the number of hexagons to that of pentagons.

The local magnetic field can be provided by the introduction of an NMR active element into the location of interest in a material. The chemical shifts inside C_{60} and C_{70}

97

were measured by ^{3}He to be -6.3 ppm and -28.8 ppm, respectively [7]. As expected, C_{70} produces a stronger diamagnetic shift than C_{60} as the former has a higher ratio of hexagons to pentagons than the latter.

5.2 THE UNIVERSAL DIAMAGNETIC SHIFT BY SWNT ENCAPSULATION

Now, let us look at the local magnetic properties inside the SWNTs. Since SWNTs consist of hexagon rings only, diamagnetic property of SWNTs is expected to be larger than that of fullerenes [8]. Marques et al. predicted the isotropic chemical shift of 21 ppm using *ab-initio* calculation, and 29 ppm using classical magnetic theory for a (8,0) tube residing inside (16,0) tube [9]. Many trials to measure the diamagnetic chemical shift of SWNTs failed due to ferromagnetic catalyst particles present in the samples, which broaden a NMR signal.

Using the novel magnetically purified SWNTs and 25% ^{13}C enriched fullerenes, we achieved well-resolved NMR signals for peapods as shown in figure 5.1(a). This is the first experimental proof for the diamagnetic shielding of SWNTs to our knowledge. The peak at 111.28 ppm results from encapsulated fullerenes which are diamagnetically shifted by as much as 36.9 ppm due to the magnetic shielding of the SWNT. The speculation that the peak could originate from SWNTs is ruled out due to the fact that i) empty SWNTs show an isotropic chemical shift at 118.8 ppm, as described in section 4.3, ii) the SWNT contribution to a NMR signal is calculated to be a maximum of 16%, when 25% ^{13}C enriched C_{60} is filled with the minimum efficiency of 70% as confirmed by

98

XRD, and iii) 4.5 ppm FWHM of the peak is simply too sharp to originate from SWNTs. Another speculation may then arise, the fullerenes corresponding to the peak at 111 ppm may be attached to the outside of the SWNTs or introduced in the interstitial channels in SWNT bundles, and not encapsulated within SWNTs. This can also be ruled out due to the fact that i) post-filling anneal treatment at 650 °C for 1 hour must have removed all of the non-encapsulated fullerenes, ii) the size of the interstitial channels in SWNT bundles is too small for fullerenes to enter, which was indeed confirmed by the constant (1,1) XRD peak position after C_{60} filling, and iii) TEM micrographs shows well-filled SWNT bundles with very little or no C_{60} on the surface.

Figure 5.1.(b) shows ^{13}C MAS NMR of peapods produced at Berkeley. Despite a different SWNT purification method and a different C_{60} encapsulation process than one followed by us, the universal diamagnetic shift is observed at 112.15 ppm.
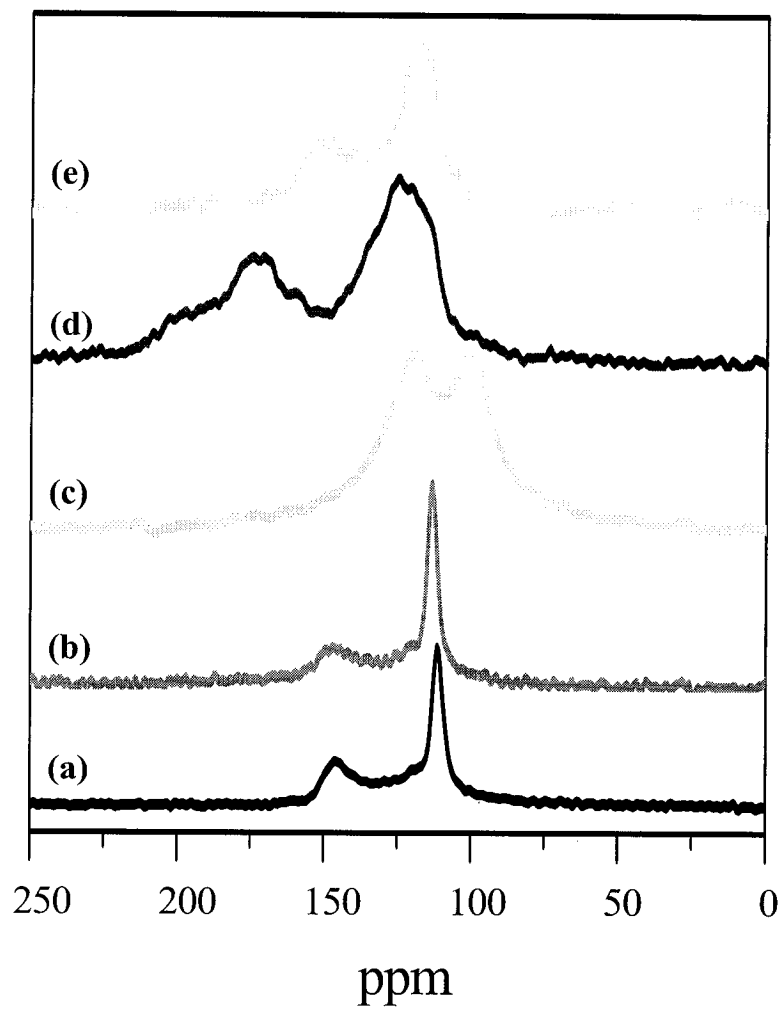
FIGURE 5.1 High resolution ^{13}C MAS NMR spectra of peapods spun at 10 KHz, for (a) peapod samples from UPENN, (b) peapods from Berkeley, (c) DWNTs transformed from peapods, (d) Rb doped peapods and (e) hydrogenated peapods.

5.3 TUNING OF THE UNIVERSAL DIAMAGNETIC SHIFT

5.3.1 TUNING BY CONTROLLING DEFECTS

We shall now investigate about the origin of the peak at 148 ppm with FWHM of 10 ppm in figures 5.1(a) and 5.1(b). The peak position is similar to that of bulk fullerenes, i.e. 143 ppm, leading to a speculation that excessive fullerenes are the origin of the peak. However, all excessive fullerenes must have been removed during the post-filling anneal process. Also, FWHM of ~ 10 ppm is too broad to be originated from freely rotating fullerenes. Instead, the peak is believed to originate from paramagnetically shifted encapsulated fullerenes due to defects. The simulation by López-Urías et al. indeed shows that defects on SWNTs such as vacancies, holes, or Stone-Wales transformations, can produce huge paramagnetic currents, even large enough to lead to ferromagnetic properties [11].

The universal diamagnetic shift by SWNT encapsulation and its dependence on defects are also observed in DWNTs as shown in figure 5.1(c). The earlier NMR measurements on DWNTs by Singer et al. produced one broad peak with FWFM of ~ 100 ppm, contrary to the prediction of two NMR peaks at ~ 100 ppm and ~ 130 ppm [9, 12]. Those two potential peaks may not have been easily resolved due to remaining ferromagnetic catalyst particles in their sample. Here, we report, for the first time, the well separated NMR peaks in the DWNTs. As expected, the peak at 99.18 ppm is responsible for the diamagnetically shifted inner nanotubes. The other peak at ~ 120 ppm

101

is deconvoluted into peaks for the outer nanotubes at 118.8 ppm and the paramagnetically shifted inner nanotubes at 125.8 ppm. As explained in chapter 4.5.2 in detail, the magnitude of diamagnetic shifts depends on the content of defects on outer SWNT walls. Intact SWNT walls produce full diamagnetic ring currents, while partially healed defects during the annealing process produce weak paramagnetic currents. Therefore, we can tune the diamagnetic shift by controlling the content of defects. A detailed study of the relationship between the oxidation time and the magnitude of a diamagnetic shift is needed and such a study is open for future research investigations.

5.3.2 TUNING BY CONTROLLING FUNCTIONALIZATION

The diamagnetic shielding of SWNTs can be controlled not only by defects, but also by functionalization. ^{3}He inside the C_{60}^{6-} anion is reported to experience stronger magnetic shielding than in neutral C_{60} by as much as $\sim$ 40 ppm [6, 13-15]. The added electrons change the total electronic structure of fullerenes such that all paramagnetic currents flowing on the pentagons become diamagnetic currents. To the contrary, ^{3}He feels weaker magnetic shielding inside C_{70}^{6-} anion than in neutral C_{70} by as much as $\sim$ 40 ppm. In this case, the added electrons make the diamagnetic currents on the hexagons weaken, and the paramagnetic currents strengthen.

Figures 5.1(d) and 5.1(e) show ^{13}C MAS NMR spectra of hydrogenated and Rb doped peapods, respectively. Rb doped peapods were prepared as follows. The peapods were pre-annealed in a homemade breakseal glass tube at 500 °C for 1 hour under a

dynamic vacuum of 10^{-6} Torr. The tube was transferred into a glove box to load Rb without breaking the vacuum using a stop-cock. The tube was pumped out again under 10^{-3} Torr with a liquid-nitrogen cold trap. The Rb was purified inside the tube by evaporation using a gentle flame before the glass tube was sealed carefully. The doping was conducted by annealing the peapods and Rb at 200 °C and 180 °C for 2 days, respectively. Finally, the doped peapods in the glass tube were transferred into an NMR glass tube under vacuum.

The universal diamagnetic shift exists in both samples with different magnitude. The hydrogenated peapods show 34.28 ppm of diamagnetic shift, whereas the Rb doped SWNTs show as much as 68 ppm of diamagnetic shift. The different magnitude of the magnetic shielding may result from a different electron doping level on SWNTs. To study this further, we have carried out Raman measurements (using Renishaw 1000 Raman spectrometer operating with a green laser at 514 nm) on bare SWNTs and Rb doped SWNTs. With the Rb doping, the RBM band at ~ 160 cm^{-1} vanishes (see figure 5.2(a)), and the G band at 1540 cm^{-1} is red-shifted by 30 cm^{-1} (figure 5.2(b)), which implies the high doping level of the SWNTs, which is close to the stage 1 (KC_8) graphite intercalated compounds (GICs) [16]. The enhanced aromaticity due to the added electrons on the π orbital in the doped SWNTs produces the larger diamagnetic shift.
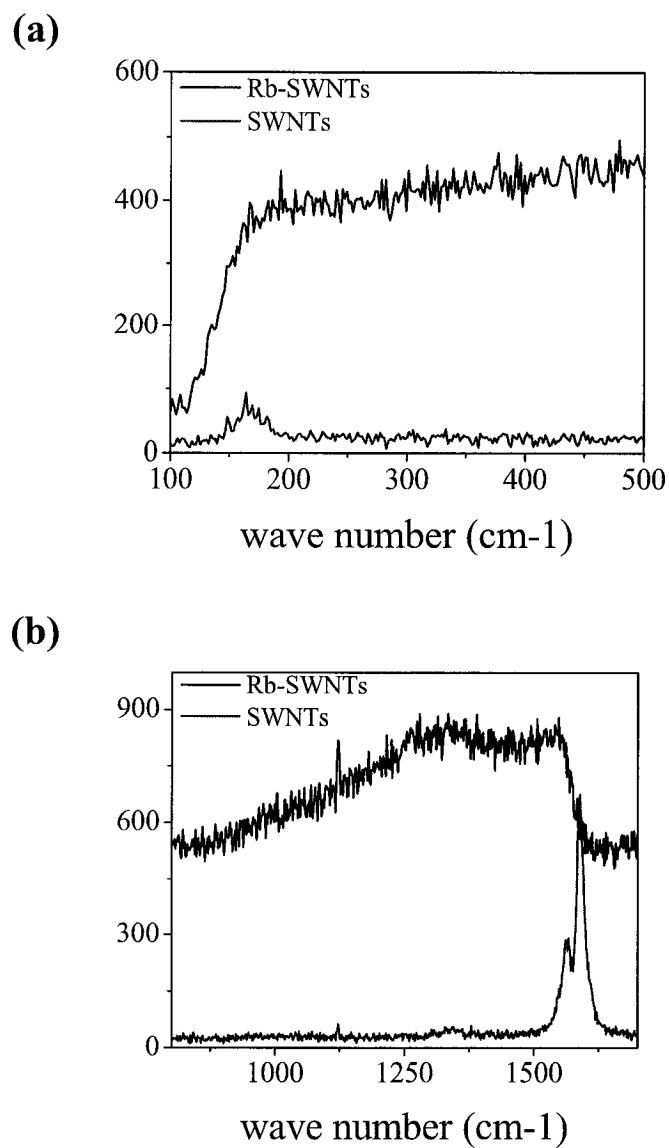
(a)

(b)

FIGURE 5.2 Raman spectra of as-received SWNTs (blue) and Rb doped SWNTs (black). (a) RBM vanishes after Rb doping. (b) G band is red-shifted by Rb doping by 30 cm^{-1}.

The hydrogenation seemed to be successful for C_{60} only, and not for SWNT at the current experimental conditions. The hydrogenation of fullerenes in peapods resulted in the broadening of each peak at 145 ppm and 111 ppm, probably due to the restriction of the free rotation of fullerenes. They may have been polymerized as shown in the small peak at ~ 20 ppm corresponding to sp^3 carbon. However, the constant peak position and width of SWNT peak before and after hydrogenation (not shown here) indicates that the SWNTs were not hydrogenated. Stability of hexagons on SWNTs will make hydrogenation more difficult than in fullerenes containing less-stable pentagons. The non-hydrogenated SWNTs in hydrogenated peapods would result in the same diamagnetic shift as those of normal peapods.

5.4 CONCLUSIONS

SWNTs are shown to produce universal diamagnetic shielding. More interestingly, the magnitude of the shielding can be tuned by controlling defects or the doping level. Defects tend to destroy magnetic shielding as they produce paramagnetic ring currents. Electron doping, instead, enhances diamagnetic shielding by increasing aromaticity of encapsulating SWNTs. The current studies have shown that SWNTs can be used as a tunable nano-magnetic shielder and they may find use in future memory or medical fields.

1. H. W. Kroto, J. R. Heath, S. C. O'Brien, R. F. Curl, and R. E. Smalley, Nature, **318**,162 (1985).

2. P. W. Fowler, P. Lazzaretti, and R. Zanasi, Chem. Phys. Lett. **165**, 79 (1990).

3. R. C. Haddon, L. F. Schneemeyer, J. V. Waszczak, S. H. Glarum, R. Tycko, G. Dabbagh, A. R. Kortan, A. J. Muller, A. M. Mujsce, M. J. Rosseinsky, S. M. Zahurak, A. V. Makhija, F. A. Thiel, K. Raghavachari, E. Cockayne , and V. Elser, Nature **350**, 46 (1991).

4. A. Pasquarello, M. Schlüter, and R. C. Haddon, Science **257**, 1660 (1992).

5. A. Pasquarello, M. Schlüter, and R. C. Haddon, Phys. Rev. A **47**, 1783 (1993).

6. R. C. Haddon, and A. Pasquarello, Phys. Rev. B **50**, 16459 (1994).

7. M. Saunders, H. A. Jiménez-Vázquez, R. J. Cross, S. Mroczkowski, Darón I. Freedberg, and F. A. L. Anet, Nature **367**, 256 (1994).

8. Y. Kim, O. N. Torrens, J. M. Kikkawa, E. Abou-Hamad, C. Goze-Bac, and D. E. Luzzi, Chem. Mater., **19** (12), 2982 (2007).

9. M. A. L. Marques, M. d'Avezac, and F. Mauri, Phy. Rev. B **73**, 125433 (2006).

10. K. Matsuda, T. Hibi, H. Kadowaki, H. Kataura, and Y. Maniwa, Phys. Rev. B **74**, 073415 (2006).

11. F. López-Urías, J. A. Rodríguez-Manzo, E. Muñoz-Sandoval, M. Terrones, and H. Terrones, Opt. Mater., **29**, 110 (2006).

12. P. M. Singer, P. Wzietek, H. Alloul, F. Simon, and H. Kuzmany, Phys. Rev. Lett. **95**, 236403 (2005).

13. M. Bühl, W. Thiel, H. Jiao, P. v. R. Schleyer, M. Saunders, and F. A. L. Anet, J. Am. Chem. Soc. **116**, 6005 (1994).

14. P. R. Birkett, M. Bühl, A. Khong, M. Saunders, and R. Taylor, J. Chem. Soc., Perkin Trans. **2**, 2037 (1999).

15. G. Wang, B. R. Weedon, M. S. Meier, M. Saunders, and R. J. Cross, Org. Lett. **2**, 2241 (2000).

16. A. M. Rao, P. C. Eklund, Shunji Bandow, A. Thess, and R. E. Smalley, Nature **388**, 257 (1997).

17. H. Alloul1, V. Brouet, E. Lafontaine, L. Malier, and L. Forro, Phys. Rev. Lett. **76**, 2922 (1996).

CHAPTER 6

SUMMARY AND FUTURE EXPERIMENTS

6.1 SUMMARY

In this thesis, the local magnetic properties of SWNTs, the 1-D dynamics of C_{60} fullerenes encapsulated in SWNTs, and the electronic properties of inner nanotubes in DWNTs were investigated using NMR spectroscopy and other techniques. In order to obtain SWNTs free from ferromagnetic catalyst particle, which are critical for NMR measurements, we developed a novel magnetic purification approach, by which 99% of ferromagnetic particles were removed, as described in chapter 3. The natural carbon based purified SWNTs produced a well-resolved ^{13}C NMR peak at 118.8 ppm with FWHM of 18.80 ppm.

In chapter 4 and 5, the local magnetic fields of SWNTs were investigated using ^{13}C enriched fullerenes as a NMR probe. With diamagnetic ring currents, SWNTs were found to screen applied magnetic fields by 36.9, 26.62, and 68.0 ppm in peapods, DWNTs, and Rb doped peapods, respectively. Paramagnetic ring currents induced from local electrons at defect sites destroy the diamagnetic shielding. The added electrons in Rb-doped peapods, instead, enhance the shielding by increasing aromaticity in encapsulating SWNTs. This study has shown that SWNTs can be used as a tunable nano-magnetic shielder. The tunability can be achieved through the control of defects in SWNTs and also by doping experiments.

In chapter 4.4.2, the dynamics of 1-D fullerenes encapsulated in SWNTs was investigated. The dynamics transition temperature from free rotation to hindered rotation in 1-D fullerenes lowered by as much as ~ 160 K compared to that in 3-D solid. The decrease of Van der Waals and Coulomb interaction among fullerenes, which results from the reduction of the nearest neighbors, results in the huge change in the temperature.

In chapter 4.5, the electronic properties of inner nanotubes in DWNTs were investigated. The universal diamagnetic shift of 26.62 ppm was obtained from two well resolved isotropic chemical shifts. In DWNT samples, 75% of the inner nanotubes were found to be metallic due to a strong interaction between inner and outer nanotubes.

6.2 FUTURE EXPERIMENTS

In chapter 4.4.1, the reason why fullerenes close to defects on SWNTs were frozen even at room temperature is not understood well. Defects could provide a stable geometry for fullerenes to rest as they break the perfect symmetry of SWNTs. Localized electrons at defects may have catalyzed the polymerization of C_{60} during the production of peapods as reported by several groups [1,2]. In order to verify the second possibility in our current studies, low temperature Raman spectroscopy or XRD can be applied [1,3].

In chapter 4.4.2, the 1-D fullerenes were found to change their dynamics from free rotation to hindered rotation at ~ 100 K. The investigation of crystal structures using synchrotron XRD and differential scanning calorimetry (DSC) will provide further better

understanding of interactions between neighboring fullerenes as well as between SWNTs and fullerenes [4].

In chapter 5, the magnetic shielding of SWNTs was shown to depend on defects and doping. In order to quantify the tunability of the magnitude, the diamagnetic shielding can be measured as a function of alkali-metal doping time and oxidation time in the air. Also one could tailor make nanotube based materials for certain magnetic shielding applications

The separate magnetic shielding effect from metallic and semiconducting SWNTs needs to be investigated for future applications [5]. Metallic tubes can be selectively damaged or removed by electrical breakdown method developed by Collins et al. [6]. The remaining "semiconducting" SWNTs may produce a discernable change in a NMR spectrum compared to that from conventional SWNTs.

Further ^{3}He-NMR studies on SWNTs or peapods could provide more detailed local magnetic properties of SWNTs. The fullerenes cannot probe the local magnetic properties in interstitial sites or grooves inside the SWNT bundles [7], while, ^{3}He has no limitation on accessing such sites.

1. H. Kataura, Y. Maniwa, M. Abe, A. Fujiwara, T. Kodama, K., Kikuchi, H. Imahori, Y. Misaki, S. Suzuki, and Y. Achiba, Appl. Phys. A: Mater. Sci. Process. A **74**, 349 (2002).

2. J. Cambedouzou, S. Rols, R. Almairac, and J.-L. Sauvajol, H. Kataura, and H. Schober, Phys. Rev. B **71**, 041403 (2005).

3. M. S. Dresselhaus, G. Dresselhaus, and P. C. Eklund, *Science of fullerenes and carbon nanotubes*, Academic press, California, (1996).

4. P. A. Heiney, J. E. Fischer, A. R. McGhie, W. J. Romanow, A. M. Denenstein, J. P. McCauley Jr., A. B. Smith, and D. E. Cox, Phys. Rev. Lett. **66**, 2911 (1991).

5. S. Latil, L. Henrard, C. Goze Bac, P. Bernier, and A. Rubio, Phys. Rev. Lett. **86**, 3160 (2001).

6. P. G. Collins, M. S. Arnold, and P. Avouris, Science **292**, 706 (2001).

7. S. E. Weber, S. Talapatra, C. Journet, A. Zambano, and A. D. Migone, Phys. Rev. B **61**, 13150 (2000).

APPENDIX A

VAN HOVE SINGULARITIES IN SWNTs

The electronic structures of SWNTs have unique van Hove singularities as mentioned in Chapter 2.1.1 and the detailed derivation is described as following.

The density of states is the number of allowed K states between E and $E+dE$ which is given by,

$$D(E)dE = \left(\frac{a}{2\pi}\right)^3 \int_{shell} d^3K \qquad (A.1)$$

where a is the lattice constant and the integral is performed over the entire shell as shown in the figure A.1.
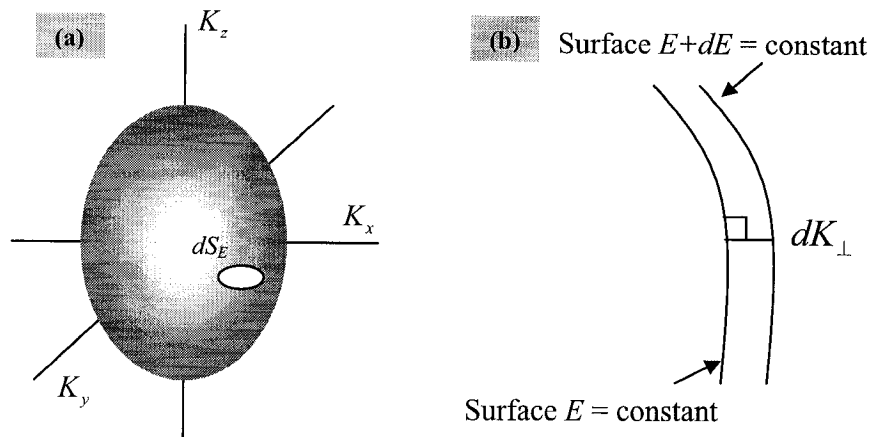

FIGURE A.1 Energy dispersion in K space. (a) Element of area dS_E on a constant energy surface in K space [1]. (b) $dK_\perp$ is the distance between two surfaces; one at constant energy E and the other at $E+dE$ [1].

The element of volume between E and $E+dE$ is a cylinder of base dS_E and altitude $dK_\perp$, resulting in

$$\int_{shell} d^3K = \int dS_E dK_\perp \qquad (A.2)$$

The magnitude of the gradient of E is the difference in energy between the two surfaces connected by $dK_\perp$, which can be expressed as

$$\left| \nabla_K E \right| dK_\perp = dE \qquad (A.3)$$

Equation A.2 is then,

$$\int dS_E dK_\perp = \int dS_E \frac{dE}{\left| \nabla_K E \right|} \qquad (A.4)$$

From equations A.1 and A.4, the density of states is given by

$$D(E) = \left(\frac{a}{2\pi} \right)^3 \int \frac{dS_E}{\left| \nabla_K E \right|} \qquad (A.5)$$

In order to figure out the DOS of SWNTs, we need to refer to the energy dispersion relation of a graphene layer as shown in figure A.2 [2-4].
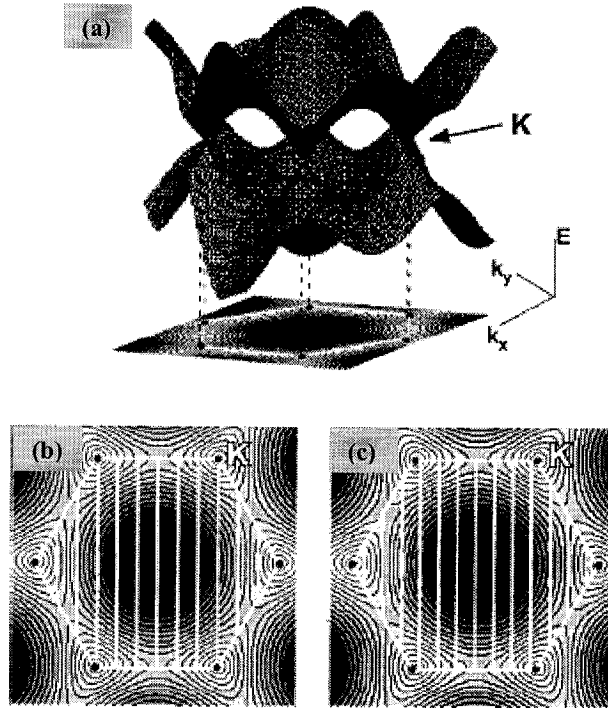
113

FIGURE A.2 Energy dispersion of a graphene layer in K space. (a) $\pi / \pi *$ energy band structure of a graphene and its 2D projection on the bottom [3]. (b) In metallic SWNTs, quantized k values displayed as white vertical lines pass through K points [3]. (c) In semiconducting SWNTs, allowed 1D sub-bands do not match K values [3].

Graphene is a semi-metal where the energy gap in K points is zero as shown in figure A.2 (a). When it is rolled into a SWNT, the wavevector k in radial direction is quantized by the criterion

$$\vec{C}_h \cdot \vec{k} = 2\pi q \qquad (A.6)$$

where $\vec{C}_h = n\vec{a}_1 + m\vec{a}_2$ and q is an integer. The quantization now makes 1D sub-bands, such that a SWNT is metallic when a sub-band passes through K points (Fig. A.2(b)), otherwise it is semiconducting (Fig. A.2(c)).

114

Figure A.3(a) shows a zoomed image near one of the K points in figure A.2(c). Since DOS will be degenerate when the gradient of energy, $\nabla_k E$, is zero as shown in equation A.5, DOS of the semiconducting SWNT would show sharp peaks at the band edges of all sub-bands as shown in figure A.3(b). These peaks in DOS are called Van-Hove singularity [5].
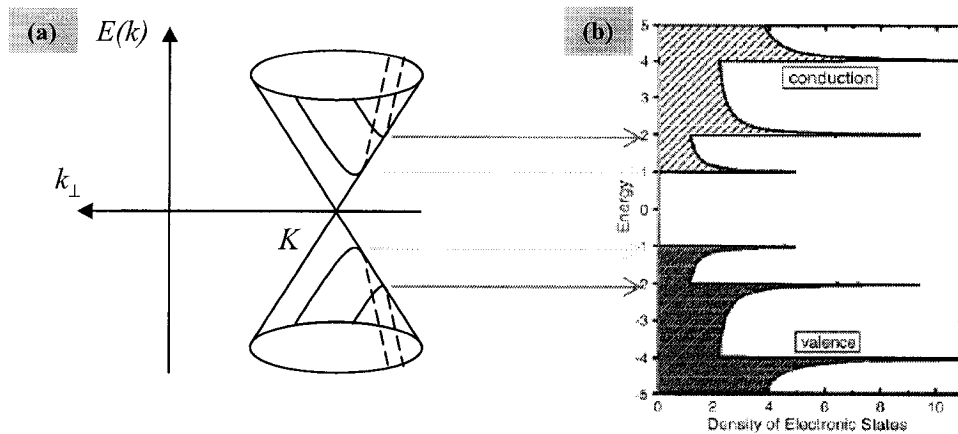

FIGURE A.3 Van Hove singularities in a semiconducting SWNT. (a) A closer look at one of the K points. (b) DOS would be degenerate at the edges of each sub-band [6].

1.   C. Kittel, *Introduction to solid state physics*, John Wiley & Sons, Inc., New York (1996).

2.   P. R. Wallace, Phys. Rev. **71**, 622 (1947).

3.   T. W. Odom, J.-L. Huang, P. Kim, and C. M. Lieber, J. Phys. Chem. Soc. B **104**, 2794 (2000).

4.   R. Saito, M. Fujita, G. Dresselhaus, and M. S. Dresselhaus, Appl. Phys. Lett. **60**, 2204 (1992).

5.   L. Van Hove, Phys. Rev. **89**, 1189 (1953).

6.   S. M. Bachilo, M. S. Strano, C. Kittrell, R. H. Hauge, R. E. Smalley, and R. Bruce Weisman, Science **298**, 2361 (2002).

APPENDIX B

MAGNETOSTATICS

In chapter 2.1.4, magnetic properties of SWNTs were described in order to explain the diamagnetic shift by SWNT encapsulation. The following is the basic magnetostatics used to obtain equation (2.6), (2.9), and (2.10).

B.1 LORENTZ'S LAW

A charge Q moving with the velocity, v, experiences force F under an electric field E and magnetic field B given by

$$F = Q\left[E + (v \times B)\right] \tag{B.1}$$

When a charge Q moves to the right along the nanotube axis under a magnetic field applied into the paper, it would be forced to move counter-clockwise unless there is an electric field as shown in figure B.1. In SWNTs under a magnetic field applied perpendicular to their axis, diamagnetic ring currents due to π electrons are induced to flow counter-clockwise, which will, in turn, induce a magnetic field opposed to the applied magnetic field.
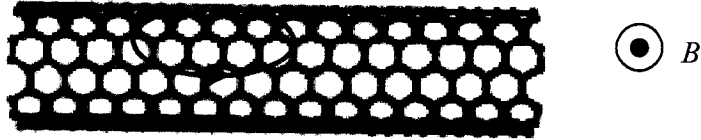
FIGURE B.1 Lorentz's law.

B.2 BIOT-SAVART LAW AND AMPÈRE'S LAW

The magnetic field induced from a steady line current is expressed by Biot-Savart law,

$$B(r) = \frac{\mu_0}{4\pi} \int \frac{I \times \hat{\eta}}{\eta^2} dl' = \frac{\mu_0}{4\pi} I \int \frac{dl' \times \hat{\eta}}{\eta^2} \qquad (B.2)$$

where μ_0 is permeability of free space, I is the steady current, dl' is an element of length along the current, and $\hat{\eta}$ is the unit vector from the source to the point r. Similarly, the magnetic fields from surface ($K(r')$) and volume currents ($J(r')$) are given by

$$B(r) = \frac{\mu_0}{4\pi} \int \frac{K(r') \times \hat{\eta}}{\eta^2} da' \text{ and } B(r) = \frac{\mu_0}{4\pi} \int \frac{J(r') \times \hat{\eta}}{\eta^2} d\tau' \qquad (B.3)$$

When currents have appropriate symmetry, Ampère's law can be used to calculate induced magnetic fields in a much easier way than with Biot-Savart law. The simple Ampère's law is given by,

$$\nabla \times B = \mu_0 J \qquad (B.4)$$

Using Stokes' theorem, the Ampère's law is converted to integral form.

118

$$\int (\nabla \times B) \cdot da = \oint B \cdot dl = \mu_0 \int J \cdot da = \mu_0 I_{enc} \qquad (B.5)$$

For example, let us calculate the induced magnetic fields inside a SWNT under an external magnetic field parallel to the nanotube axis as shown in figure B.2(a). The clockwise surface currents would be induced if the SWNT is metallic. As shown in figure B. 2 (b), Ampère's law can be applied to loop 1, resulting in

$$\oint B \cdot dl = [B(a) - B(b)] L = \mu_0 I_{enc} = 0 \qquad (B.6)$$

Since there is no surface current enclosed in loop 1,

$$B(a) = B(b) \qquad (B.7)$$

The magnetic field outside the SWNT does not depend on the distance, meaning that both B(a) and B(b) are zero.

Now, Ampère's law is applied to loop 2 to give

$$\oint B \cdot dl = B_{in} L = \mu_0 I_{enc} = \mu_0 KL \qquad (B.8)$$

where K is the induced surface current on the SWNT. Finally, we can get the induced magnetic field B_{ind} expressed as,

$$B_{ind} = \begin{cases} \mu_0 K \hat{z}, & \text{inside the SWNT}, \\ 0, & \text{outside the SWNT}. \end{cases} \qquad (B.9)$$

When an external magnetic field is applied parallel to the metallic SWNT axis, the induced magnetic field inside the tube due to the induced surface current is uniform and parallel to the applied magnetic field.
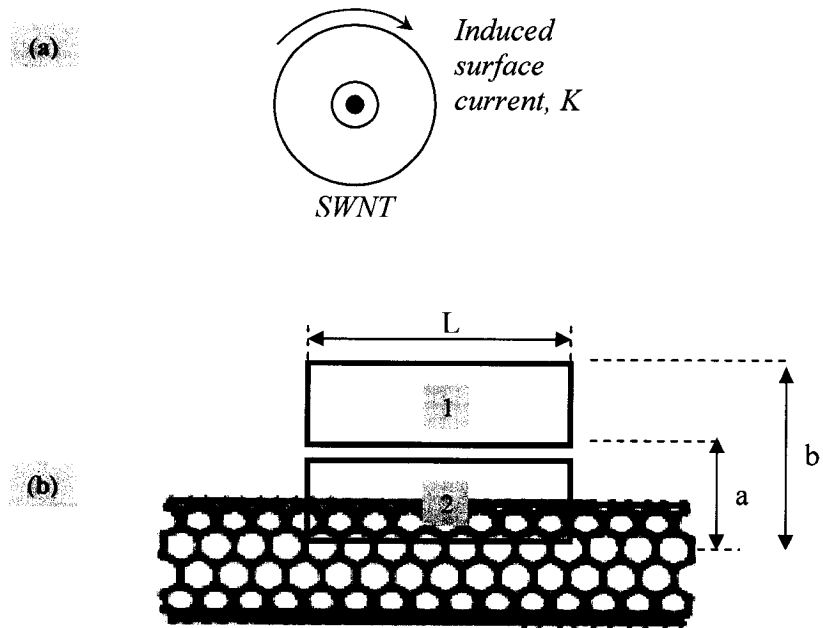
119

FIGURE B.2 Induced magnetic field inside a SWNT under a magnetic field. (a) Induced current flows clockwise in a metallic SWNT under a magnetic field applied into the paper. (b) Ampère's law. See the text for details.

1. D. J. Griffiths, *Introduction to electrodynamics*, Prentice Hall International, Inc., New Jersey (1999).

APPENDIX C

ISOTROPIC CHEMICAL SHIFT IN NMR

The motion averaged chemical shift in an isotropic liquid expressed in equation (2.19) is derived as following.

The orientation of a molecule in 3-dimensional space can be specified using 3 Euler angles, α, β, and γ. When positive rotation is applied, the Euler rotation matrix $R(\alpha, \beta, \gamma)$ is expressed as,

$$R(\alpha, \beta, \gamma) = \begin{pmatrix} \cos\alpha\cos\beta\cos\gamma - \sin\alpha\sin\gamma & -\sin\alpha\cos\gamma - \cos\alpha\cos\beta\sin\gamma & \cos\alpha\sin\beta \\ \sin\alpha\cos\gamma + \cos\alpha\sin\gamma & \cos\alpha\cos\gamma - \sin\alpha\cos\beta\sin\gamma & \sin\alpha\sin\beta \\ -\sin\beta\cos\gamma & \sin\beta\sin\gamma & \cos\beta \end{pmatrix} \quad \text{(C.1)}$$

where α, β, and γ are the rotations about the original z axis, the new y axis, and the final z axis, respectively.

The chemical shift tensor of a molecule with orientation (α, β, γ) is then expressed as,

$$\delta^j(\alpha, \beta, \gamma) = R(\alpha, \beta, \gamma)\delta^j(0,0,0)R(-\gamma, -\beta, -\alpha) \quad \text{(C.2)}$$

where $\delta^j(0,0,0)$ is given by,

$$\delta^j = \begin{pmatrix} \delta^j{}_{xx} & \delta^j{}_{xy} & \delta^j{}_{xz} \\ \delta^j{}_{yx} & \delta^j{}_{yy} & \delta^j{}_{yz} \\ \delta^j{}_{zx} & \delta^j{}_{zy} & \delta^j{}_{zz} \end{pmatrix} \quad \text{(C.3)}$$

The average chemical shift tensor of a molecule over all the orientations is given by,

$$\overline{\delta^j(\alpha, \beta, \gamma)} = \frac{1}{8\pi^2} \int_0^{2\pi} d\alpha \int_0^{\pi} d\beta \sin\beta \int_0^{2\pi} d\gamma \delta^j(\alpha, \beta, \gamma) \quad \text{(C.4)}$$

Since the off-diagonal of the average chemical shift tensor, for example $\left(\overline{\delta^j(\alpha,\beta,\gamma)}\right)_{zx}$,

is zero, the isotropic chemical shift is the same as the zz component of the average

chemical shift tensor under a magnetic field applied to the z-axis as shown in the

following equation.

$$\left(\overline{\delta^j(\alpha,\beta,\gamma)}\right)_{zz} = \delta_j^{iso} = \frac{1}{3}(\delta_{xx}^j + \delta_{yy}^j + \delta_{zz}^j) \qquad (C.5)$$

where δ_{xx}^j, δ_{yy}^j, and δ_{zz}^j are the three diagonal elements of $\delta^j(0,0,0)$.

1.   M. H. Levitt, *Spin dynamics-basics of nuclear magnetic resonance,* John Wiley & Sons, LTD, New York, (2001).

2.   M. Mehring, Princiles *of high resolution NMR in solids,* Springer-Verlag, Berlin Heidelberg, New York, (1983).